

PCCP

Accepted Manuscript



This is an *Accepted Manuscript*, which has been through the Royal Society of Chemistry peer review process and has been accepted for publication.

Accepted Manuscripts are published online shortly after acceptance, before technical editing, formatting and proof reading. Using this free service, authors can make their results available to the community, in citable form, before we publish the edited article. We will replace this *Accepted Manuscript* with the edited and formatted *Advance Article* as soon as it is available.

You can find more information about *Accepted Manuscripts* in the [Information for Authors](#).

Please note that technical editing may introduce minor changes to the text and/or graphics, which may alter content. The journal's standard [Terms & Conditions](#) and the [Ethical guidelines](#) still apply. In no event shall the Royal Society of Chemistry be held responsible for any errors or omissions in this *Accepted Manuscript* or any consequences arising from the use of any information it contains.

The local structure of $\text{Pd}_x\text{Ce}_{1-x}\text{O}_{2-x\delta}$ solid solutions

Cite this: DOI: 10.1039/x0xx00000x

R.V. Gulyaev¹, T.Yu. Kardash^{1,2}, S.E. Malykhin¹, O.A. Stonkus^{1,2}, A.S. Ivanova¹, A.I. Boronin^{1,2*}

Received 00th January 2012,
Accepted 00th January 2012

DOI: 10.1039/x0xx00000x

www.rsc.org/

$\text{Pd}_x\text{Ce}_{1-x}\text{O}_{2-x\delta}$ solid solutions, which are highly efficient catalysts for the low-temperature oxidation of carbon monoxide, were examined using a set of structural (XRD-PDF, HRTEM, XRD) and spectral (XPS, Raman spectroscopy) methods in combination with quantum-chemical calculations. A comparison of the experimental results and pair distribution function (PDF) modeling data enabled reliable verification of the model of non-isomorphic substitution of Ce^{4+} ions by Pd^{2+} ions in $\text{Pd}_x\text{Ce}_{1-x}\text{O}_{2-x\delta}$ solid solutions. Palladium ions were shown to be in a near square planar environment with C_{4v} symmetry, which is typical for Pd^{2+} ions. Such a near square planar environment was revealed by Raman spectroscopy due to the appearance of the band with $\omega = 187 \text{ cm}^{-1}$, which corresponds to the A_1 vibrational mode of Pd^{2+} ions in $[\text{PdO}_4]$ subunits. The binding energy of $\text{Pd}_{3d_{5/2}}$ ($E_b(\text{Pd}_{3d_{5/2}})$) for the Pd^{2+} ion in the CeO_2 lattice is 1 eV higher than that of $E_b(\text{Pd}_{3d_{5/2}})$ for PdO oxide due to a decrease in the Pd-O distances and the formation of more ionic bonds because of the displacement of Pd^{2+} ions with respect to the position of Ce^{4+} ions in the fluorite structure. Five structural models of solid solutions are considered in the work. As demonstrated by the DFT calculations, the most realistic model is based on the displacement of palladium ions leading to a PdO_4 near square planar environment, which includes water molecules stabilizing the region of anion vacancy in their dissociated state as two hydroxyl groups. The introduction of water molecules in the composition of the $\text{Pd}_x\text{Ce}_{1-x}\text{O}_{2-x\delta}$ solution leads to a decrease in the formation energy and to additional stabilization of palladium in the CeO_2 matrix. The formation of $\text{Pd}_x\text{Ce}_{1-x}\text{O}_{2-x\delta}$ solid solutions is accompanied by the dispersing effect caused by distortions of the fluorite structure stimulated by Pd^{2+} ions. The coprecipitation method, which allows Pd^{2+} ions to be introduced at the stage of fluorite structure formation, was demonstrated to be the most optimal for the synthesis of a homogeneous $\text{Pd}_x\text{Ce}_{1-x}\text{O}_{2-x\delta}$ solid solution.

1 Introduction

Among all lanthanides, only cerium has two stable oxidation states, +4 and +3. This feature underlies the unique properties of its highest oxide CeO_2 , in particular, the ability to change the oxygen content in its structure without a phase transition¹⁻⁷. This oxygen storage capacity (OSC) makes CeO_2 the virtually irreplaceable basis for a broad class of heterogeneous catalysts. In addition, ceria is capable of the labile substitution of Ce^{4+} ions in its structure by cations of other metals, which strongly modifies the structure and changes the properties of the resulting doped oxide. In particular, the effect of increasing the oxygen mobility, OSC value and thermal stability upon introduction of Ti^{4+} , Zr^{4+} , Hf^{4+} ⁸⁻¹², Sn^{4+} ¹³, Co^{2+} ^{14,15} and Gd^{3+} ^{16,17} ions as well as other ions of rare-earth elements (RE)¹⁸ into the ceria lattice is well known. Such modification of ceria is related to structural distortions of the fluorite phase produced

by the dopant cations. For isovalent ions, for example Zr^{4+} , Sn^{4+} or RE ions, Ce^{4+} ion is isomorphically substituted by an ion of the corresponding dopant; this process decreases the lattice parameter of the doped ceria and facilitates the removal of oxygen ions from tetrahedral positions of CeO_2 ¹⁹. Vegard's law holds true for the region of existence of the $\text{Ce}_{1-x}\text{M}_x\text{O}_2$ solid solution⁸, i.e., the lattice parameter of the solid solution decreases linearly as a function of the concentration of a metal substituent if its cationic radius is less than the radius of the Ce^{4+} ion. The phase diagrams, electronic structure and catalytic properties of such solutions have been studied thoroughly for $\text{Ce}_{1-x}\text{Zr}_x\text{O}_2$ mixed oxides in experimental^{3,9,20} and theoretical^{21,22} works.

Some works have demonstrated that platinum group metals are prone to a similar strong interaction with ceria; among these metals are rhodium^{19,23,24}, platinum²⁵⁻²⁷, and palladium^{25,28-41}. This phenomenon may lead also to the formation of solid

solutions, which is accompanied by a substantial increase in the oxygen mobility and OSC value. Such materials are promising for application in heterogeneous catalysis. The most pronounced enhancement of catalytic properties is observed for the solid solutions containing palladium and ceria. However, the exact structure of $\text{Pd}_x\text{Ce}_{1-x}\text{O}_{2-\delta}$ solid solutions and the valent state of palladium in their composition are still not clear. In contrast to Zr^{4+} ions, which isomorphically substitute cerium ions, Pd^{2+} ions are characterized by a square planar environment, which is atypical of the fluorite structure of CeO_2 . Nevertheless, a similar isomorphous substitution of Ce^{4+} ions by palladium ions is assumed in the majority of experimental studies^{33,42-45}. Considering the smaller radius of Pd^{2+} ion (0.64 Å) compared with Ce^{4+} ion (0.97 Å), the formation of isomorphous substitutional solutions would decrease the lattice parameter of the solid solution according to Vegard's law. However, the XRD experiments revealed a considerable growth of the lattice parameter of the solid solution upon increasing the palladium content. As the palladium concentration is increased, the lattice parameter of the $\text{Pd}_x\text{Ce}_{1-x}\text{O}_{2-\delta}$ solid solution increases linearly from $a = 5.411$ Å for pure CeO_2 to $a = 5.417$ Å⁴³ and $a = 5.416$ Å⁴⁴ for the $\text{Pd}_{0.1}\text{Ce}_{0.9}\text{O}_{2-\delta}$ stoichiometry and $a = 5.455$ Å for the $\text{Pd}_{0.2}\text{Ce}_{0.8}\text{O}_{2-\delta}$ stoichiometry⁴⁵. In⁴³, such an increase in the lattice parameter is attributed to the growth of mutual repulsion of cations caused by the removal of a part of oxygen from the solution lattice because the Ce^{4+} cation is substituted by a Pd^{2+} cation with a smaller charge. The authors of⁴⁴ report that an increase in the lattice parameter is related to the formation of additional Ce^{3+} ions and oxygen vacancies upon the introduction of palladium into the CeO_2 lattice. Ce^{3+} ions, which have a larger radius (1.23 Å) than Ce^{4+} ions, would increase the lattice parameter of the solid solution. In⁴⁵, such an increase in the lattice parameter of the solid solution was attributed to both the increase in the concentration of anion vacancies and the decrease in the crystallite sizes with increasing palladium content in $\text{Pd}_x\text{Ce}_{1-x}\text{O}_{2-\delta}$ solid solutions. The locally sensitive EXAFS method revealed the presence of three Pd-Element distances in the lattice of 1%Pd/ CeO_2 catalyst ($\text{Ce}_{0.99}\text{Pd}_{0.01}\text{O}_{1.9}$ solid solution), 2.02, 2.73 and 3.31 Å. In³³, these distances were interpreted as the Pd-O, Pd-Pd and Pd-Ce distances within the model of isomorphous substitution of cerium ions by palladium ions in the CeO_2 lattice. An EXAFS study of the 2%Pd/ CeO_2 sample⁴⁰ revealed two distances, 1.98 and 3.18 Å. The first one was interpreted as the Pd-O distance in the $[\text{PdO}_4]$ square planar complexes on the CeO_2 surface, and the second one was interpreted as the Pd-O-Ce distance. These conclusions were based on the model of the surface Pd-O-Ce superstructure calculated in³⁷ using the DFT method. Investigation of the 5%Pd/ CeO_2 sample⁴⁶ revealed distances equal to 1.6 and 3.2 Å, which were also attributed to Pd-O and Pd-O-Ce distances in compliance with the data reported in⁴⁷; no structural model of the local environment of palladium ion was proposed there. The authors of⁴⁷ supposed the formation of Pd-O-Ce bonds because the binding energy of $\text{Pd}3d_{5/2}$ level in the XP spectra was increased with respect to PdO, and the

DW factors were increased in the description of the EXAFS curves.

There is no generally accepted quantum-chemical model of the $\text{Pd}_x\text{Ce}_{1-x}\text{O}_{2-\delta}$ solid solution^{13,22,41,42,48-53}. The authors of⁵⁰ reported the formation of the $\text{Pd}_{0.03}\text{Ce}_{0.97}\text{O}_2$ substitutional solution, a where Pd^{2+} ion occupies the position of a cerium ion and has the coordination number of 8. Doping with palladium decrease the formation energy of the oxygen vacancy from 2.4 to 0.59 eV. This decrease accompanied by the reduction of Ce^{4+} to Ce^{3+} and Pd^{2+} to Pd^{1+} . In contrast, in⁴⁸ it was stated that the Pd^{2+} ion was displaced from the cerium ion position by 1.3 Å to form a $[\text{PdO}_4]$ planar square; this process leads to the spontaneous formation of a charge-compensating oxygen vacancy. The calculated formation energy of the oxygen vacancy in this solution is 173 kJ/mol (~ 1.8 eV) compared with 253 kJ/mol (2.6 eV) in pure CeO_2 . Upon formation of the oxygen vacancy, two adjacent cerium ions are reduced to Ce^{3+} , while the palladium ion retains its oxidation state of 2+. The authors of³⁷ also calculated a model of the Pd-O-Ce surface superstructure, where Pd^{2+} ions replace cerium ions and a square planar environment is retained, residing on the $\{110\}$ surface of CeO_2 and forming the chain structures along the $[001]$ direction. This process is accompanied by the formation of charge-compensating surface vacancies and low-coordinated oxygen ions.

Thus, our literature analysis of recent experimental and theoretical works demonstrated the absence of commonly accepted opinion. Therefore, we used a complex of physical methods in combination with quantum chemistry calculations to study the local structure of $\text{Pd}_x\text{Ce}_{1-x}\text{O}_{2-\delta}$ solid solutions. The quantum-chemical methods employed in our work are based on density functional theory. Quantum-chemical calculations are combined only with the physical methods that are sensitive to the local structure of a substance. Among such methods is the pair distribution function (PDF) obtained by the Fourier transform of the normalized X-ray diffraction scattering measured for a wide range of scattering vectors. The PDF curve shows the distribution of interatomic distances⁵⁴. Because both Bragg scattering and diffuse scattering are considered, this method becomes a powerful tool for investigating disordered materials, liquids and nanosystems⁵⁵⁻⁵⁷. For ceria-based materials, the modeling of PDF curves measured by pulsed neutron diffraction has revealed the presence of interstitial oxygen defects, which are related to OSC⁵⁸. In addition, the indicated approach proved to be efficient in the study of Ce- ZrO_2 nanostructured oxides and ceria doped with rare-earth metals⁵⁹. Thus, it seemed reasonable to apply the PDF method for the analysis of bulk $\text{Pd}_x\text{Ce}_{1-x}\text{O}_{2-\delta}$ solid solutions. To perform a comprehensive structural characterization of $\text{Pd}_x\text{Ce}_{1-x}\text{O}_{2-\delta}$ solid solutions, we also used a complex of informative physical methods: X-ray diffraction analysis (XRD), high resolution transmission electron microscopy (HRTEM), X-ray photoelectron spectroscopy (XPS), and Raman spectroscopy.

2 Experimental

2.1 Catalyst synthesis

IWI SERIES. The 8.2-wt%Pd/CeO₂ catalysts were synthesized using incipient wetness impregnation (IWI). The CeO₂ support was prepared by precipitation from a cerium nitrate solution followed by drying and calcination in air at 450°C for 4 h. Palladium was supported by incipient wetness impregnation from a Pd(NO₃)₂ nitrate solution. The samples were dried and then calcined in air at 450, 600 and 1000°C.

CP SERIES. Coprecipitation was used to obtain the Pd-CeO₂ solid solution with the same Pd loading 8.2-wt%. First, Ce(NO₃)₃ and Pd(NO₃)₂ solutions were mixed; this step was followed by precipitation with a 1N KOH aqueous solution at pH 8.8-9.0 and room temperature with subsequent aging under the same conditions for 2 h. The precipitates obtained by filtering were dried in air and then at 110°C for 12-14 h. The dried samples were calcined in flowing air at 450°C for 4 h; potassium was then removed by washing with subsequent calcination in air at 450, 600 and 1000°C.

In addition, we examined a pure CeO₂ support, which was used for the synthesis of IWI catalysts.

SPECIFIC SURFACE AREAS were determined with an accuracy of ±10% through the thermal desorption of argon.

2.2 XPS study

An XPS study was performed using an ES300 photoelectron spectrometer (Kratos Analytical, UK). The analyzer was calibrated against the Au4f_{7/2} (E_b = 84.0 eV) and Cu2p_{3/2} (E_b = 932.7 eV) lines of the pure metal surfaces of gold and copper. The base pressure in the spectrometer was less than 5*10⁻⁹ mbar. Before placing the samples in the spectrometer, the catalysts were ground in an agate mortar; the samples were then deposited on conductive carbon tape. Spectra were recorded at a fixed pass energy of the analyzer using a low power X-ray source (13 kV x 5 mA, 65 W) to prevent photoinduced reduction of ceria. To control the surface composition and the possible presence of impurities, the survey spectra were recorded at a pass energy of 50 eV over the binding energy range of 0 – 1100 eV with a 1 eV step. For precise analysis of the charge states of the elements, spectra of the main photoelectron lines of individual elements were recorded at a pass energy of 25 eV with an energy step of 0.1 eV. The MgK_α line was used as the primary radiation. Mathematical processing of the spectra was performed using the XPS Calc software, which was developed at the Boreskov Institute of Catalysis and tested using many catalytic systems, including ceria-based catalysts⁶⁰⁻⁶⁶. The spectra processing included subtraction of the MgK_{α3,4} satellite and subtraction of the background of inelastically scattered electrons using the Shirley method. Pd3d and Ce3d spectra were decomposed into the individual components using Gauss-Lorentz functions. The spectra were calibrated for surface charging against the U^{III} component of the Ce3d line, its binding energy was taken to be 916.7 eV⁶⁷.

2.3 XRD-PDF study

The phase composition was determined using powder X-ray diffraction (XRD) patterns which were collected on a Bruker D8 Advance diffractometer using Cu K_α radiation. The diffraction intensities were measured using a LynxEye position sensitive detector. XRD patterns were collected in the 2θ range 10-70°, with a 0.02° step size and a 2 s collection time. Phase analysis was performed using the ICDD PDF-2 database. Rietveld refinement was performed using TOPAS v4.2 software⁶⁸. The sizes of the coherent scattering domains (CSD) for constituent phases and microstrain parameters were estimated using the fundamental parameter approach⁶⁹. An external standard material — well-crystallized Si powder — was used to describe the instrumental broadening.

The diffraction data for the PDF were obtained using synchrotron radiation at the anomalous scattering beamline of the Siberian SR Center at the Budker Institute of Nuclear Physics. X-ray scattering curves were obtained using a focusing reflection geometry and a wavelength of λ = 0.6993 Å in the 2θ range of 3-138° with a 0.01° step. Thus, the upper limit of integration was Q_{max} = 16.5 Å⁻¹. The wavelength was refined against a standard corundum sample (NIST standard SRM676). The normalized scattering curves S(Q) and PDF curves were calculated using the PDFgetX2 program⁷⁰ (see equation 1).

$$G(r) = \frac{2}{\pi} \int_0^\infty Q[S(Q) - 1] \sin(Qr) dQ = 4\pi[\rho(r) - \rho_0] \quad (1)$$

where $Q = 4\pi \sin\theta/\lambda$, $\rho(r)$ is the paired atomic density (the probability of finding the *i* atom at a distance *r* from the *j* atom) and ρ_0 is the average density.

Modeling of the PDF curves was performed using the PDFgui program⁷¹. The model curve for each structure was calculated using equation (2)

$$G_{\text{cry}}(r) = \frac{1}{r} \sum_i \sum_j \left[\frac{f_i f_j}{\langle f \rangle^2} T_{ij}(r) \right] - 4\pi r \rho_0 \gamma(r) \quad (2)$$

where $T_{ij}(r)$ is the temperature factor accounting for individual atomic thermal vibrations, correlated thermal vibrations and resolution of the diffractometer.

Modeling of distances over a wide range accounted for the size effect. For distances greater than the nanoparticle diameter, the calculated G(r) curve was multiplied by the envelope function (3-4):

$$G_{\text{nano}}(r) = G_{\text{cry}}(r) f(r) \quad (3)$$

$$f(r) = \left[1 + \frac{3r}{2d} + \frac{1}{2} \left(\frac{r}{d} \right)^3 \right] \Theta(d - r) \quad (4)$$

where *d* is the diameter of a spherical particle, and the $\Theta(x)$ function is equal to 0 for *r* distances smaller than the particle diameter and 1 for interatomic distances greater than the particle diameter. The Instrumental broadening parameters, Q_{broad} and Q_{damp}, were refined for a reference sample (NIST

standard SRM676) and remained constant when refining the structural parameters.

2.4 HRTEM study

An electron microscopy investigation was performed using JEM-2010 and JEM-2200FS (JEOL Co., Japan) electron microscopes operated at 200 kV to obtain HRTEM images. The STEM HAADF mode was employed together with EDX and EELS spectroscopy. The samples for the TEM study were ultrasonically dispersed in ethanol and supported on a perforated carbon film mounted on a copper grid.

2.5 Raman spectroscopy study

The Raman spectra were obtained using a Nicolet NXR 9650 (Thermo Scientific) equipped with a NdYAG laser, 1064 nm.

2.6 Quantum-chemical calculations

The palladium-containing CeO_2 phase was modeled as two $2 \times 2 \times 2$ supercells built from the CeO_2 fcc unit cell ($a = 5.41 \text{ \AA}$). The obtained supercells correspond to $\text{PdO} \cdot (\text{CeO}_2)_{31}$ and $\text{PdO} \cdot (\text{CeO}_2)_{31} \cdot \text{H}_2\text{O}$ gross formulas. The optimal geometry calculations were performed within a self-consistent density functional theory framework, as implemented in the PWSCF plane-wave pseudopotential code of the Quantum-ESPRESSO distribution. The Perdew-Burke-Ernzerhof exchange-correlation density functional was used. Ultrasoft pseudopotentials were employed in the present study. The one-electron valence wave functions and the electron density were described by plane-wave basis sets with kinetic energy cutoffs of 25 and 300 Ry, respectively. The reciprocal space was approximated by Gamma-point.

3 Results and discussion

3.1.1 XRD data

The X-ray diffraction patterns of the samples synthesized by coprecipitation (CP) and impregnation (IWI) are presented in Fig. 1. The most intense peaks in the diffraction patterns correspond to the ceria phase with the fluorite structure (ICDD PDF-2 # 34-0394). No other phases were detected in the coprecipitation samples calcined at 450 and 600°C. The microstructural parameters were determined using the Rietveld refinement. The experimental, calculated and difference curves are plotted in Fig. 1. The diffraction patterns of the CP-450 and 600 samples were described using only the fluorite CeO_2 cell. The main contribution to the diffraction pattern of such nanosized compounds was caused by the size effect and broadening of the diffraction profile due to microdistortions; thus, the occupancy of positions was refined only in the last step and did not produce a substantial decrease in the R_{wp} values. A thorough analysis of the calculated and experimental profiles revealed slight disagreements in the intensities of reflections (for example, the 222 and 400 reflections); however, due to the large width of the lines, a description of the average structure within the fluorite phase yields R_{wp} values equal to 4%.

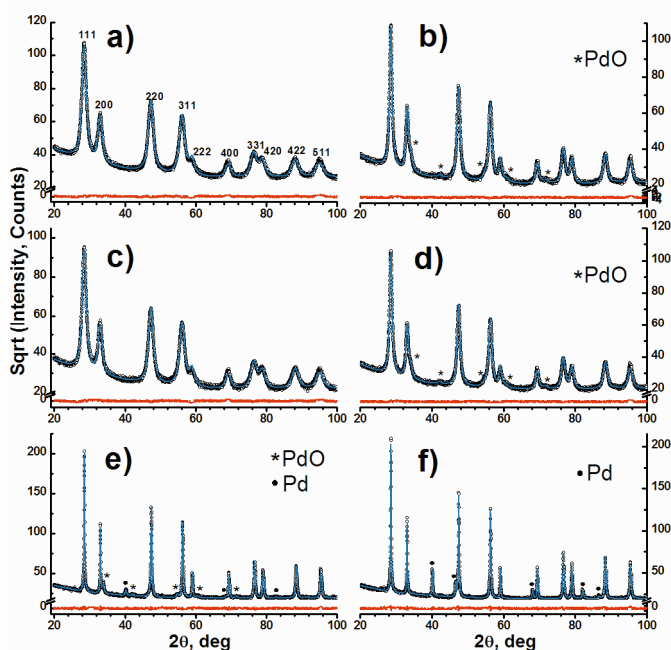


Fig. 1. X-ray diffraction patterns for CP-450 (a), CP-600 (c) and CP-1000 (e) samples and IWI-450 (b), IWI-600 (d) and IWI-1000 (f) samples. Fit from "normal" CeO_2 fluorite-type structure. The experimental curves are represented by black circles, the fits are represented by blue solid lines, and the difference curves are shown below (red). The intensities are displayed as \sqrt{I} .

Thus, the standard approach to the analysis of diffraction patterns is insensitive to changes in the local structure, which are related to the incorporation of palladium into the ceria structure. Calcination of these samples at 1000°C leads to the appearance of Bragg maxima corresponding to the phases of palladium oxide (ICDD PDF-2 #41-1107) and metallic palladium (ICDD PDF-2 # 46-1043). The CSD size of the PdO phase is $14.6 \pm 0.6 \text{ nm}$, and that of metallic palladium is $18 \pm 1 \text{ nm}$. The presence of microstrains was not considered when estimating the particle size of the palladium-containing phases.

The samples synthesized by impregnation and calcined at 450°C (IWI-450) initially consist of two phases. Together with the main ceria phase, a palladium oxide phase was also present, whose CSD size was equal to $5.2 \pm 2 \text{ nm}$ and only slightly changed when the calcination temperature was increased to 600°C. Calcination of the samples at 1000°C resulted in the disappearance of palladium oxide and the appearance of metallic palladium. The particle size of metallic palladium is quite large: according to estimates obtained by modeling the diffraction profile, the CSD size is $35 \pm 1 \text{ nm}$.

Table 1 lists data on the phase composition of the tested samples, the cell parameters of the fluorite phase, and their CSD size and microstrains. A comparison of the diffraction patterns for two series of samples with the same content of palladium indicates that, in contrast to the IWI- samples, the CP- samples are monophasic, with their average structure being adequately described within the fluorite structure of CeO_2 . The lattice parameter of the fluorite phase in CP samples is greater

than in the IWI samples. Such an increase in the lattice parameter was reported earlier⁴³⁻⁴⁵ when discussing solid solutions of Pd in CeO₂. However, in the CP-450 and CP-600

samples the CSD size of the CeO₂ phase is 6 – 7 nm versus 11–12 nm for IWI-450 and IWI-600 samples.

Table 1. Phase composition of Pd-CeO₂ samples synthesized by coprecipitation and impregnation. Structural and microstructural characteristics of the phase with a fluorite structure

T _{calc.} , °C	CP				IWI			
	Phases	a, Å	particle size, nm	microstrains	Phases	a, Å	particle size, nm	microstrains
450	CeO ₂	5.4349(3)	6.3(1)	0.232(5)	CeO ₂ , PdO	5.4169(2)	11.5(1)	0.107(3)
600	CeO ₂	5.4333(3)	7.0(1)	0.228(5)	CeO ₂ , PdO	5.4158(2)	11.7(2)	0.106(3)
1000	CeO ₂ , PdO, Pd	5.41231(4)	92(2)	0.034(1)	CeO ₂ , Pd	5.41187(4)	74.7(1)	0.007(1)

Calcination of the samples at 1000°C leads to the appearance of metallic palladium and palladium oxide phases for the coprecipitated samples. Upon formation of palladium-containing phases, the unit cell parameters of the fluorite phase approach each other for the coprecipitated and impregnated samples. Although the CSD size in coprecipitated sample after calcination at 1000° is higher than that of the impregnated sample, the amount of microstrains is greater in the first sample. This fact and the retained PdO phase in the CP samples indicate a pronounced interaction of palladium with ceria in the CP samples calcined at low temperatures.

3.1.2 HRTEM data

HRTEM examination of the CP-450 sample revealed that its structure is represented only by ceria nanodomains with particle sizes of 5–10 nm. Nanoparticles of PdO oxide and metallic palladium were not detected (Fig. 2.a).

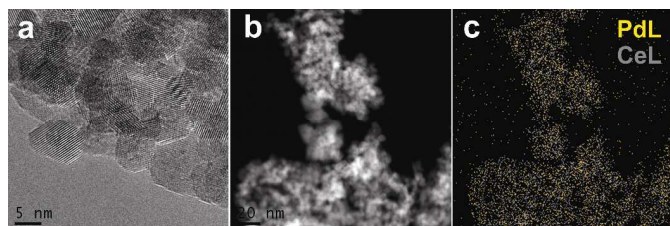


Fig. 2. a) HRTEM image of CP-450 catalyst area, b) HAADF STEM image of a large area of CP-450 catalyst, c) EDX mapping of the same area in (b) obtained from CeL and PdL emission lines.

However, EDX mapping of the CP-450 sample area, using the CeL and PdL emission lines, demonstrated that palladium uniformly distributed over the entire area (Fig. 2.b,c). Palladium nanoparticles were not detected in this area. Considering the high concentration of palladium in this sample, palladium is most likely dissolved in the ceria lattice.

For the IWI-450 sample, the particle size distribution of CeO₂ is also quite uniform with particles sizes of 10 – 20 nm (Fig. 3.a). However, high resolution images reveal numerous nanoparticles with sizes of 1.5 nm and smaller. Note that obtaining an image of the crystal lattice of such clusters is difficult due to their small size. However, in some cases, it is possible to detect the interplanar spacing related to palladium in the metallic state. We believe that the metallic state is formed

under the *in situ* effect of the electron beam. Under the ambient air, the metallic clusters are likely partially oxidized to PdO_x.

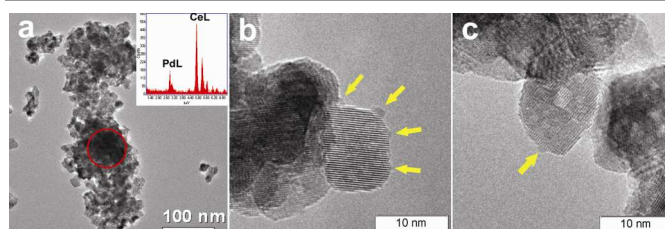


Fig 3. a) BF TEM image of IWI-450 catalyst. b) and c) BF HRTEM images of IWI-450 catalyst areas with PdO_x nanoparticles on ceria surface, marked by arrows.

In the studied IWI samples, some of the palladium was concentrated in the form of PdO particles comprising PdO-CeO₂ agglomerates, wherein the PdO particles were located predominantly in the center of the agglomerates. These HRTEM results are in consistent with the XRD data presented above.

Thus, in comparison with the CP-450 sample, IWI-450 has, on average, a twofold greater particle size for the fluorite phase and contains some PdO nanoparticles

3.1.3 Raman spectroscopy data

Raman spectroscopy was employed to analyze the CP-450 sample and compare it with pure CeO₂. For IWI catalysts synthesized by impregnation, the application of Raman spectroscopy was hindered by a strong adsorption of the primary laser radiation and pronounced heating of the sample. The spectra are presented in Fig. 4. The main peak at 450–460 cm⁻¹ corresponds to the F_{2g} vibrational mode of oxygen ions in the [CeO₈] cubic subunit of the CeO₂ structure⁷²⁻⁷⁵. The bands at 550 and 600 cm⁻¹, which are weakly pronounced for pure CeO₂ and more intense for the CP-450 sample, are assigned to the so-called defect-induced vibrational mode (D-mode), and the band at 250 cm⁻¹ is the transverse second-order acoustic vibrational mode (2TA). For pure ceria, the main band is narrow, and its Raman-shift is equal to 463 cm⁻¹, which is typical of pure ceria. The width of the main F_{2g} line is determined by phonon confinements effects and depends on the mean size of the crystal domain. The size of the ceria crystallite, as estimated from the FWHM of the F_{2g} peak by the formula reported in⁷³, is 15.6 nm (Table 3). The Raman spectrum recorded for the CP-450 sample differs from the

spectrum of pure ceria mainly by the main peak of the F_{2g} vibrational mode, which is strongly broadened and shifted to 455 cm^{-1} . This effect is caused by the smaller size of the crystalline domains of the fluorite phase due to the introduction of palladium into the ceria structure. The crystalline domain size determined from the Raman spectrum is 4.6 nm (Table 3). A similar shift and broadening of the F_{2g} peak for $\text{Pd}_x\text{Ce}_{1-x}\text{O}_{2-\delta}$ solid solutions was observed in ⁴⁵. The additional band at 187 cm^{-1} observed for the CP-450 sample was also reported in ⁴⁵.

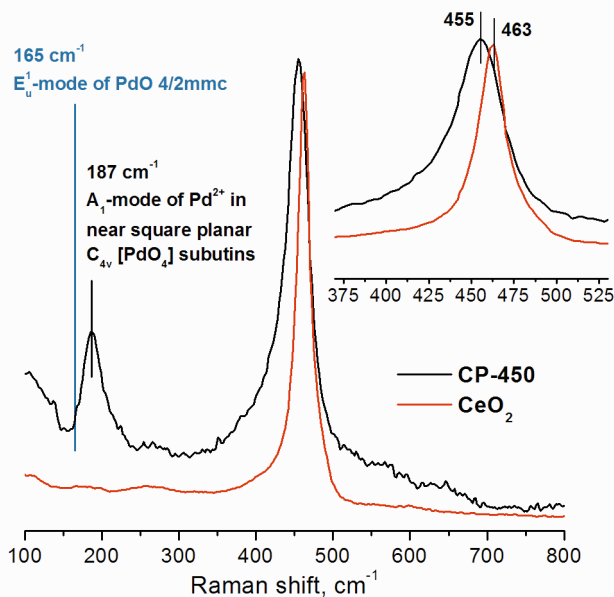


Fig. 4. Raman spectra obtained for CP-450 catalyst and pure ceria. Raman-forbidden E_{u}^1 band position for nanocrystalline PdO is shown on the graph taken from ref. ⁷⁶.

Note that palladium oxide is characterized by an intense band at 651 cm^{-1} in the Raman spectrum, which corresponds to the B_{1g} vibrational mode of square planar $[\text{PdO}_4]$ subunits in the palladium oxide structure ⁷⁶. The absence of the corresponding band in the spectrum for the CP-450 sample allows the assignment of the band at 187 cm^{-1} to the PdO phase to be excluded. It can be concluded that the band at 187 cm^{-1} cannot be attributed to palladium oxide; however, its partial contribution coincides with the molar content of palladium with respect to cerium. Thus, this band most likely be assigned to palladium cations located in the ceria structure.

3.1.4 XPS data

For the samples calcined at 450 and 600°C , the charge state of palladium on the surface obtained by analysis of the Pd3d doublet line corresponds to the oxidized state. For the CP-450 sample, the state of palladium is essentially uniform and represented by the $\text{Pd}3d_{5/2}$ component with $E_b(\text{Pd}3d_{5/2}) = 338.0\text{ eV}$ (Fig. 5.a). Note that the binding energy of the $\text{Pd}3d_{5/2}$ line for PdO oxide is in the range of $336.7 - 337.0\text{ eV}$ ⁷⁷⁻⁷⁹; thus, the observed binding energy of the $\text{Pd}3d_{5/2}$ line for the CP-450 sample strongly exceeds the value typical of PdO. In addition,

such an increased value of the binding energy is typical of Pd/CeO₂ catalysts ^{12,25,33,41,43,44,46}. The elevated value of $E_b(\text{Pd}3d_{5/2})$ is caused by localization of individual palladium ions in the ceria lattice ^{12,25,33,42,43,44}. Earlier, we also observed the increased position of Pd3d level with respect to PdO in Pd/CeO₂ catalysts ^{60,62,63}, which was assigned to Pd²⁺ ions in the $\text{Pd}_x\text{Ce}_{1-x}\text{O}_{2-\delta}$ substitutional solid solution. In addition, the Pd3d spectrum of the CP-450 sample also contains an additional low-intensity component with $E_b(\text{Pd}3d_{5/2}) = 336.1\text{ eV}$, which cannot be attributed to PdO nanoparticles. Note that these additional palladium species on the surface of Pd/CeO₂ catalysts are not considered in the literature. However, such states of palladium are very important for the low-temperature oxidation of CO over Pd/CeO₂ catalysts ⁶³. At the current stage of our study, the exact composition and structure of such states of palladium are not quite clear; nevertheless, we believe that these oxidized palladium structures are close to small PdO_x clusters that are anchored on the surface defects of ceria.

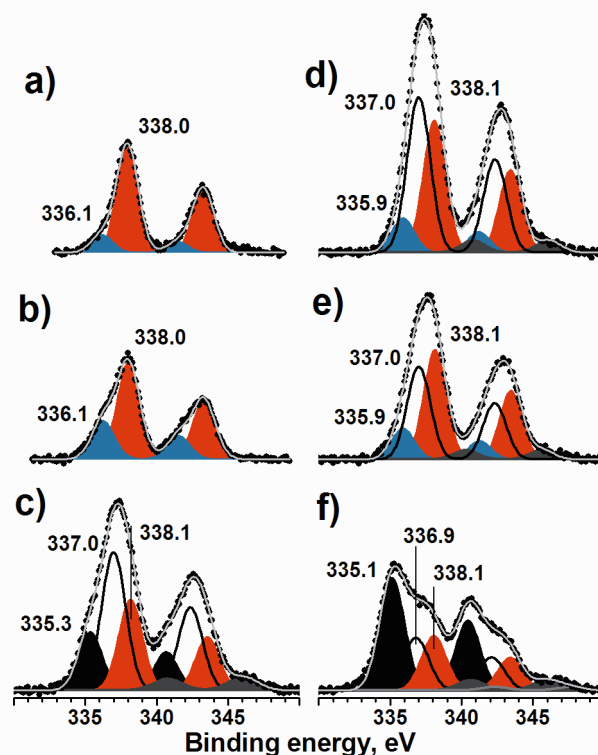


Fig. 5. Pd3d spectra obtained for CP-450 (a), CP-600 (b), CP-1000 (c), IWI-450 (d), IWI-600 (e), and IWI-1000 (f) samples. All the spectra are normalized to the integral intensity of the Ce3d photoelectron line.

For the CP-600 sample, the main state of palladium also corresponds to the $\text{Pd}_x\text{Ce}_{1-x}\text{O}_{2-\delta}$ solid solution (Fig. 5b); however, the intensity of the additional state with the binding energy 336.1 eV is much higher compared with the sample calcined at 450°C . It cannot be ruled out that these structures are the products of Pd²⁺ ions segregation from the solid solution lattice during calcination.

For the samples synthesized by impregnation, the corresponding Pd3d lines are strongly broadened (Fig. 5d,e).

Note that the widths of the C1s, O1s and Ce3d photoelectron lines (Fig. 6) were virtually identical for all the tested samples, both impregnated and coprecipitated. Thus, the broadening of the Pd3d line for the IWI samples can only be attributed to the presence of additional states of palladium.

Fixation of the parameters of the Gauss–Lorentz functions and decomposition of the spectra (see Table S1) reliably indicate the presence of three components in the Pd3d lines for IWI samples. The component with $E_b(\text{Pd}3d_{5/2}) = 338.1$ eV (Fig. 5d,f) corresponds to the $\text{Pd}_x\text{Ce}_{1-x}\text{O}_{2-\delta}$ solid solution. In our opinion, the state with $E_b(\text{Pd}3d_{5/2}) = 335.9$ eV can be interpreted similar to the case of the CP-450 samples. For the IWI-450 sample, the most intense component with the binding energy of 337.0 eV (Fig. 5d) corresponds to palladium oxide. Earlier, we observed the same value for the Pd3d level of sintered Pd/CeO₂ samples containing PdO nanoparticles⁶⁰. The presence of palladium oxide is also confirmed by the presence of shake-up satellites near 341 and 346 eV in the XP spectra of the IWI-450 and IWI-600 samples. The presence of such shake-up satellites in XP spectra is typical of PdO oxide^{78,79}. Note that such satellites are not observed in XP spectra of the samples synthesized by coprecipitation. Increasing the calcination temperature to 600°C decreases the intensity of the component corresponding to PdO oxide (Fig. 5f). This effect may be related to both the sintering of PdO nanoparticles and their dissolution in ceria yielding the $\text{Pd}_x\text{Ce}_{1-x}\text{O}_{2-\delta}$ solid solution.

Calcination of samples from both series at 1000°C resulted in the decomposition of the solid solution into palladium oxide, PdO, and metallic palladium. This effect is observed as the appearance of components with $E_b(\text{Pd}3d_{5/2}) = 337.0 - 336.9$ eV, which corresponds to PdO, and $E_b(\text{Pd}3d_{5/2}) = 335.3 - 335.1$ eV, which is assigned to metallic palladium. For the IWI-1000 sample, the metallic state of palladium on the surface is the main state, while for the CP-1000 sample the main state is represented by the oxide. For the CP-1000 sample, palladium oxide appears to be the decomposition product of the $\text{Pd}_x\text{Ce}_{1-x}\text{O}_{2-\delta}$ solid solution, and in the IWI sample, the oxide was initially present on the surface. It is known that PdO oxide is unstable at temperatures above 850°C and decomposes into a metal⁸⁰, which was observed for the IWI-1000 sample. For the CP-1000 sample, the presence of palladium oxide on the surface may be caused only by reoxidation of metallic palladium upon cooling the sample to room temperature in air. Reoxidation of the metal produced by the decomposition of PdO was also observed for $\text{Pd}_{0.11}\text{Ce}_{0.89}\text{O}_{2-y}$ solid solutions by *in situ* XRD⁴⁵. Thus, the calcination of $\text{Pd}_x\text{Ce}_{1-x}\text{O}_{2-\delta}$ solid solutions at 1000°C leads to their decomposition into individual oxides. However, complete decomposition occurs neither for the introduction of palladium into the bulk of CeO₂ nor upon its surface deposition, which is evidenced by the presence of components with $E_b(\text{Pd}3d_{5/2}) = 338.1$ eV in the Pd3d spectra of CP-1000 and IWI-1000 samples.

Fig. 6 displays the C1s, O1s and Ce3d spectra for samples CP-450 and IWI-450. In both cases, the O1s line consists of three components. The main component with $E_b(\text{O}1s) = 529.6$ eV

corresponds to the anion sublattice oxygen. It is observed that the binding energy does not depend on the introduction of palladium into the CeO₂ lattice; moreover, the same binding energy is observed for the O1s level for pure CeO₂. Thus, the O1s spectra indicate that the charges on the O²⁻ ions remain unchanged upon the introduction of palladium into the structure of CeO₂. A component with $E_b(\text{O}1s) = 531.8$ –531.9 eV is assigned to the adsorbed surface compounds (hydroxides and carbonates). For the CP-450 sample, the fraction of these oxygen species is greater than on the surface of the IWI-450 sample. A component with $E_b(\text{O}1s) = 534.5$ eV is attributed to the Pd3p_{3/2} line. For the C1s line, one observes not only the main peak with the binding energy of 285.3 eV, which corresponds to species of elementary carbon but also a component with $E_b(\text{C}1s) = 288.9$ –289.1 eV, which is ascribed to surface carbonates; the fraction of this state is greater for the CP-450 sample.

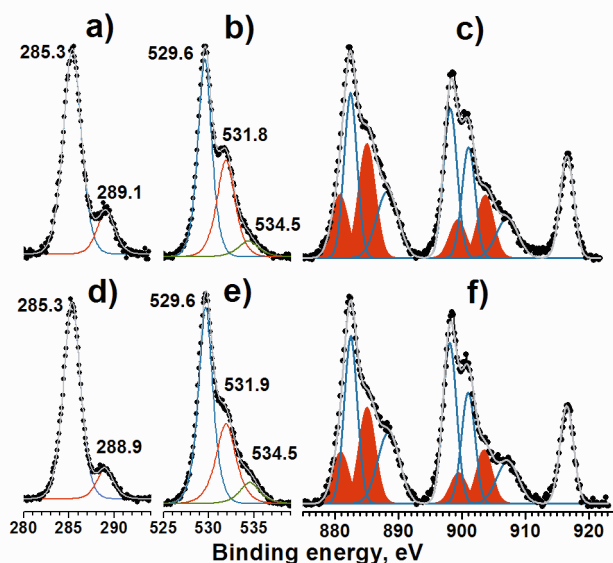


Fig. 6. C1s (a, d), O1s (b, e) and Ce3d (c, f) spectra obtained for CP-450 and IWI-450 samples. Spectra a-c were obtained for the CP-450 sample; spectra d-f were obtained for IWI-450 sample.

The decomposition of the Ce3d line into five doublets, which allows the fraction of Ce³⁺ ions to be determined⁸¹, provides evidence of the higher concentration of Ce³⁺ ions for the CP-450 sample compared with IWI-450. Quantitative data for all the tested samples are listed in Table 2. For the IWI samples, the content of trivalent cerium is virtually independent of the calcination temperature and is equal to 27–28%, whereas for samples CP-400 and CP-600 the fraction of trivalent cerium is much greater, attaining 36%. This finding indicates a higher concentration of surface defects and anion vacancies. Upon calcination at 1000°C (CP-1000 sample), the concentration of Ce³⁺ ions becomes equal to that for the IWI samples. The presence of anion vacancies is confirmed by the ratio of the O1s component with $E_b(\text{O}1s) = 529.6$ eV, corresponding to the lattice oxygen, and the total intensity of the Ce3d line. For the IWI samples, this ratio corresponds to the CeO₂ stoichiometry,

while for the CP-450 and CP-600 samples this ratio is equal to 1.3, which indicates a considerable oxygen deficiency. Note that the absolute value of this ratio is not a criterion of the exact CeO_x stoichiometry and depends on various factors. Nevertheless, the low value of this ratio for the CP sample with respect to the IWI samples unambiguously indicates oxygen depletion of the surface. Increasing the calcination temperature of the CP sample to 1000°C increases this ratio to 2.1, i.e., to the value characterizing samples from the IWI series.

Table 2. The fraction of Ce^{3+} ions, O/Ce atomic ratio, and concentration ratio of the oxygen species with $E_b(\text{O}1s) = 531.8 \text{ eV}$ to the carbon species with $E_b(\text{C}1s) = 289 \text{ eV}$ as calculated from XPS data for all the studied samples

Sample	% Ce^{3+}	O1s(529.6)/Ce3d	O1s(531.8)/C1s(289)
CP-450	34	1.3	3.1
CP-600	36	1.3	3.5
CP-1000	29	2.1	4.9
IWI-450	28	2.0	3.3
IWI-600	28	2.0	3.1
IWI-1000	27	2.0	3.8

In addition, quite a high concentration of carbonate structures was observed on the surface of the samples. For the IWI and CP samples calcined at 450 and 600°C , the ratio of the O1s line component with $E_b(\text{O}1s) = 531.8 \text{ eV}$ to the C1s line component with $E_b(\text{C}1s) = 289 \text{ eV}$ is 3.1-4.9, which may correspond to HCO_3^- and CO_3^{2-} ions.

Thus, palladium tends to dissolve in the ceria lattice with the formation of a solid solution even when palladium is deposited on the surface by impregnation. In this case, a substantial amount of palladium dissolves in the subsurface layers of CeO_2 , and the remainder remains on the surface as oxide particles. The introduction of palladium into the bulk of ceria enhances the interaction of palladium with ceria and results in its complete dissolution yielding the $\text{Pd}_x\text{Ce}_{1-x}\text{O}_{2-\delta}$ solid solution. The introduction of palladium into the bulk leads to the formation of more defect particles containing anion vacancies and a greater amount of adsorbed carbonate compounds compared with palladium deposition on the surface by impregnation. Calcination at 1000°C results in partial decomposition of the $\text{Pd}_x\text{Ce}_{1-x}\text{O}_{2-\delta}$ solid solution and the formation of metallic and oxide palladium.

3.1.5 Quantum-chemical calculations

The optimized geometry of the CeO_2 phase with intercalated Pd^{2+} ion is not presented here because it differs only slightly from the structure examined in ⁴⁸. In the resulting structure, the Pd^{2+} ion retains an environment that is close to square planar. The calculation using this model produced a zero spin density on the palladium ion, which agrees with the data reported in ⁴⁸. However, the model proposed in ⁴⁸ implies the existence of a large empty space in the lattice of such a solid solution. This space forms due to the displacement of Pd^{2+} ion from the fluorite position into the face of an O_8 cube, which leads to the square planar geometry and formation of the charge-compensating oxygen vacancy V_O . Considering that solid solutions of the CP series were synthesized in our work by coprecipitation in an aqueous medium, we assumed that this

space could be filled with a water molecule. We have found that introduction of the water molecule into the space decreases the energy by 92 kJ/mol .

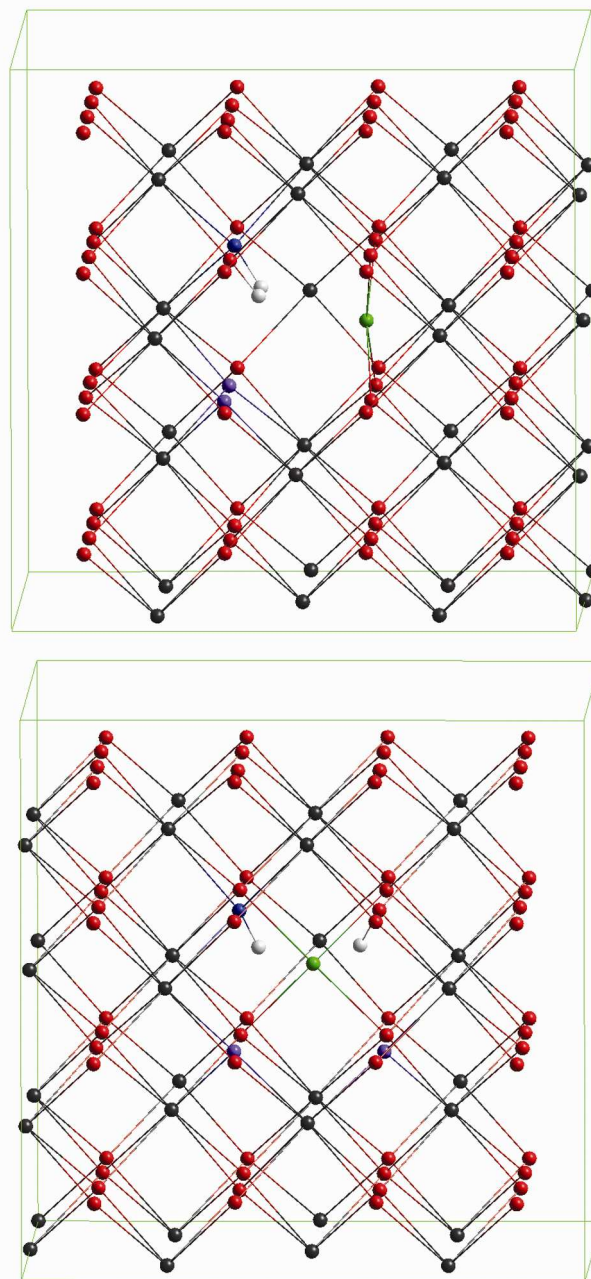


Fig. 7. Two different projections of the calculated $\text{PdO}-(\text{CeO}_2)_{31}\cdot\text{H}_2\text{O}$ supercell. The black spheres denote the cerium ions, the green sphere denotes the Pd^{2+} ion, and the red spheres represent the oxygen ions of the regular ceria lattice. The violet spheres denote the 3-coordinated O^{2-} ions, while the blue and white spheres represent the oxygen and hydrogen from the introduced water molecule, respectively.

This decrease is accompanied by dissociation of the water molecule, such that a hydroxyl ion OH^- occupies the anion vacancy and the remaining proton is added to the adjacent O^{2-} ion with the formation of a second hydroxyl. The other two O^{2-}

ions are in a threefold coordination (the violet spheres in Fig. 7), owing to which they are slightly displaced toward the bound Ce^{4+} ions along the (111) family directions. The resulting hydroxyl groups are coordinated by threefold O^{2-} ions via the formation of hydrogen bonds. Thus, the water molecule, which was introduced in the supercell to form OH^- and H^+ ions, is incorporated nearly perfectly in the regular structure of CeO_2 . Such modification of the initial supercell causes the cell parameter to remain virtually unchanged. For example, the calculated pressure tensor for a $2 \times 2 \times 2$ cell of pure CeO_2 is -8.29 kbar, while the value of this tensor for $\text{PdO} \cdot (\text{CeO}_2)_{31} \cdot \text{H}_2\text{O}$ supercell is only -4.18 kbar for the cell parameter equal to 5.41 \AA in both cases. Here, the Pd-O bond length is 1.98 \AA , which is somewhat smaller compared with PdO oxide, where this bond length is equal to 2.01 \AA . However, in the absence of distortions and the perfect square planar of Pd^{2+} environment in the fluorite structure of CeO_2 this distance would be 1.91 \AA , indicating that the Pd-O bond length in this solid solution has an intermediate value between the Pd-O bond lengths in PdO oxide and $\text{Pd}_x\text{Ce}_{1-x}\text{O}_{2-\delta}$ solid solution with undistorted lattice of CeO_2 oxide. Note that only the nearest neighbors of palladium atoms are displaced and that the overall structure of the fluorite is not disturbed and shows only minor distortions. Thus, the introduction of palladium in the ceria lattice and filling of the resulting space with water molecules is not expected to increase the lattice parameter of such a solid solution. Note that the geometry of the 1st coordination sphere of Pd^{2+} ions, exhibits a minor difference from the ideal square-planar geometry: the Pd^{2+} ion shifted from $[\text{PdO}_4]$ plane by 0.13 \AA which leads to the formation of an almost square-planar geometry or rather flattened tetrahedral pyramid $[\text{PdO}_4]$, thus the symmetry of 1st coordination sphere decreases from D_{4h} to C_{4v} .

According to the main idea of the work in ⁴⁸, the existence of under-coordinated oxygen ions in the lattice of a Pd-doped ceria would increase the OSC of such materials. As demonstrated in ⁴⁸, this effect occurs due to a decrease in the energy of oxygen vacancy formation with participation of under-coordinated ions to 173 kJ/mol compared with pure CeO_2 (253 kJ/mol). Such a process implies the formation of two adjacent anion vacancies, which would positively contribute to the formation energy of the oxygen vacancy calculated in ⁴⁸. Using the hydration energy of this solid solution equal to 92 kJ/mol , which was calculated in our work, and the formation energy of the oxygen vacancy obtained in ⁴⁸, one can estimate the formation energy of an oxygen vacancy in the hydrated $\text{PdO} \cdot (\text{CeO}_2)_{31} \cdot \text{H}_2\text{O}$ solid solution as $173 - 92 = 81 \text{ kJ/mol}$. Thus, the $\text{PdO} \cdot (\text{CeO}_2)_{31} \cdot \text{H}_2\text{O}$ solid solution is proposed to be characterized by a high OSC value, which is promising for heterogeneous oxidation catalysis.

3.1.6 PDF data

A set of physicochemical methods employed in our study has demonstrated that CP samples calcined at 450 and 600°C are single-phased and have a distorted fluorite structure with an increased lattice parameter. Palladium is distributed uniformly

over the bulk of these samples and does not form individual phases. The mean particle sizes calculated from the BET, XRD and TEM data agree well with each other. This fact excludes the formation of the domain structure where palladium could segregate within the boundaries of individual domains. All these data in combination with Raman spectroscopy and XPS data and quantum-chemical calculations indicate the formation of a Pd solid solution in the CeO_2 structure of these samples.

Table 3 lists the quantitative data on the mean particle size of the samples, which were obtained directly from HRTEM and XRD and indirectly from BET and Raman spectroscopy.

Table 3. Mean particle size obtained from BET, XRD, HRTEM and Raman spectroscopy

Sample	S_{BET} [m^2/g]	D_{BET}^* [nm]	D_{XRD} [nm]	D_{HRTEM} [nm]	D_{Raman}^{**} [nm]
CP-450	162	4.8	6.3	5-10	4.6
CP-600	146	5.4	7.0	5-10	-
IWI-450	72	10.9	11.5	10-20	-
IWI-600	70	11.2	11.7	-	-
CeO_2 -450	72	10.9	11.5	10-20	15.6

*calculated from S_{BET} using formula $D_{[\text{nm}]} = \frac{6000}{\rho_{\text{CeO}_2} [\text{g}/\text{cm}^3] \cdot S_{\text{BET}} [\text{m}^2/\text{g}]}$

**calculated from FWHM of F_{2g} peak using formula $D_{[\text{nm}]} = \frac{124.7}{\Gamma[\text{cm}^{-1}] - 10}$ from ref. ⁷³

As observed in Table 3, the data acquired by using different physical methods agree well with each other.

A more detailed structural examination of the solid solutions was performed using the X-ray PDF method. Fig. 8 displays the PDF curves for the CP-450 and CP-600 samples with respect to the curve for pure CeO_2 in the $1\text{-}8 \text{ \AA}$ range of interatomic distances. The normalized scattering curves for these samples are presented in the Supplementary section (Fig. S2). CeO_2 , which was used as the reference sample, is adequately described by the fluorite structure, allowing for a partial reduction of cerium cations, which is typical of highly dispersed samples. For charge compensation, 10% oxygen vacancies were introduced (see Fig. S3). All the maxima observed experimentally correspond to the interatomic distances in the fluorite structure; no additional maxima were detected. This result indicates the single-phase nature of the material at the local scale and confirms the formation of a solid solution of palladium in CeO_2 . However, a comparison of the positions and intensities of the maxima with pure CeO_2 as the reference sample revealed changes in the bond lengths and coordination numbers due to Pd introduction. The position and intensity of the first maximum corresponding to the Ce-O distance are similar to those of pure CeO_2 , whereas the Ce-Ce peak shifts and decreases in intensity for the solid solution samples compared with pure CeO_2 . Similar changes are also observed for the more distant coordination spheres. For the X-ray PDF curves, scattering from the cationic sublattice prevails over scattering from the oxygen atoms. Therefore, in this work, we discuss mainly the changes and disorder in the cationic

sublattice that are caused by incorporation of palladium cations in the structure of CeO_2 .

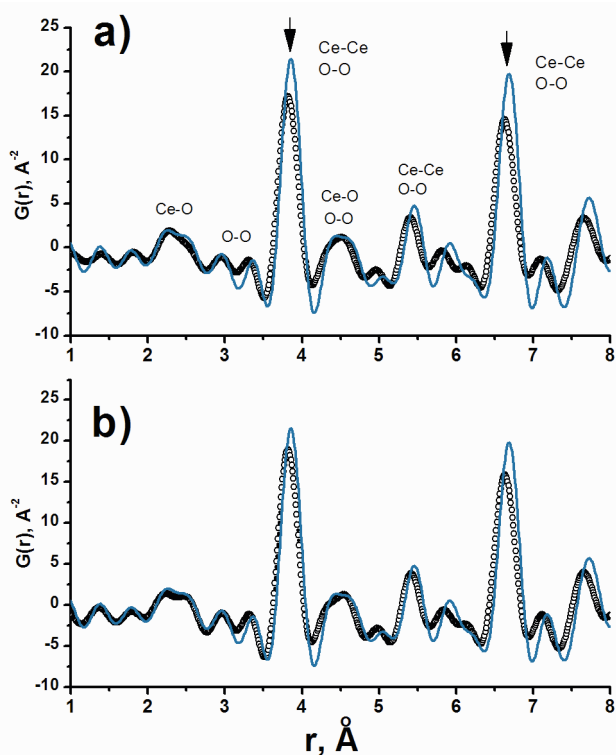


Fig. 8. Low- r region of X-ray PDFs (a) of CP-450 (circles) and CeO_2 (solid blue curve) and (b) of CP-600 (circles) and CeO_2 (solid blue curve).

Examination and refinement of the solid solution model were performed in three steps. In the first step, we selected a model by refining only the local structure in the range of distances $1 < r < 15 \text{ \AA}$, where the effects of decreasing coordination numbers due to a finite size can be neglected, thus minimizing the set of parameters to be refined. Then, the most suitable model was refined for a wide range of interatomic distances. Finally, the same model was used to refine the average structure using the Rietveld method using standard powder diffraction data. The last step was necessary to verify that, despite the palladium intercalation and distortion of the structure at the local level, the structure corresponds on average to the fluorite structure and describes a standard diffraction experiment.

Because the PDF curves for two samples exhibits no significant differences, we will consider data obtained by modeling the CP-450 sample. Data for the CP-600 sample are presented in the Supplementary section (Fig. S4).

According to the hypotheses on the structure of $\text{Pd}_x\text{Ce}_{1-x}\text{O}_{2-\delta}$ solid solutions, which are discussed in the literature, we considered two families of the models. The first family implies that the cerium cation is substituted by a palladium cation, such that palladium ion remains in the position of the cerium ion. Such models are proposed as a result of quantum-chemical calculations of the bulk⁵⁰ and surface^{22,51} of $\text{Pd}_x\text{Ce}_{1-x}\text{O}_{2-\delta}$ solid solutions; these models were used to describe experimental

EXAFS data^{13,42}. The second family implies that the substitution of cerium cation is followed by the displacement of the palladium cation from the fluorite position toward a O_8 cube face with the formation of a square planar subunit $[\text{PdO}_4]$. This family of models was not verified experimentally and is considered because of quantum-chemical modeling of the bulk $\text{Pd}_x\text{Ce}_{1-x}\text{O}_{2-\delta}$ solid solution^{48,49} and its surfaces^{37,53}. Both families of models assume the formation of anion vacancies allowing for different oxidation states of palladium and different $\text{Ce}^{3+}/\text{Ce}^{4+}$ ratios. The main difference between these two families is related to the presence or absence of the displacement of the palladium ion substituent from the corresponding position of the cerium ion. Overall, we considered five models including all combinations. In family 1, the palladium ions occupy the positions of cerium ions; this family consists of three models.

MODEL I: The anion sublattice of the parent ceria is completely retained, i.e., oxygen vacancies are absent, which formally corresponds to the gross formula $\text{Pd}_x\text{Ce}_{1-x}\text{O}_2$ ($\delta=0$), where the palladium ion is in the oxidation state 4+.

MODEL II: One adjacent oxygen vacancy per palladium ion, which corresponds to the gross formula $\text{Pd}_x\text{Ce}_{1-x}\text{O}_{2-x}$ ($\delta=x$), where the palladium ion is in the oxidation state 2+.

MODEL III: More than one oxygen vacancy per palladium ion, which formally, this corresponds to the gross formula $\text{Pd}_x\text{Ce}_{1-x}\text{O}_{2-x-y/2}$ ($\delta=x+y/2$). The palladium ion is in the oxidation state 2+, and trivalent cerium ions with the molar fraction y are present in the lattice.

In the family 2 models IV and V, the palladium ion is displaced from the cerium position along the (100) direction to attain a geometry close to the square planar one. In view of the square planar environment, the hypotheses with palladium ions in the oxidation state 4+ were not considered in models of this family.

MODEL IV: This model based on model III. The corresponding formula is $\text{Pd}_x\text{Ce}_{1-x}\text{O}_{2-x-y/2}$ ($\delta=x+y/2$); the molar fraction of the Ce^{3+} ions is equal to y , and there is one oxygen vacancy per Pd^{2+} ion in the perfect square-planar geometry.

MODEL V: This model is based on the geometry of the local environment of the palladium ion, which was obtained by quantum-chemical calculations. One water molecule per Pd^{2+} ion in near square planar geometry is introduced into the lattice. The water molecule fills the charge-compensating oxygen vacancy with the formation of two hydroxyl groups. The corresponding formula is $\text{Pd}_x\text{Ce}_{1-x}\text{O}_{2-x-y/2} \cdot x\text{H}_2\text{O}$ ($\delta=x+y/2$); the molar fraction of Ce^{3+} ions is equal to y .

A schematic representation of all these models is presented in Fig. 9. To construct the atomic model, we built a $3 \times 3 \times 3$ supercell from CeO_2 unit cells, where the cerium atoms were randomly substituted with palladium atoms with a specified probability $x = 13\%$ which corresponded to the molar concentration of palladium. Then, depending on the family of models, palladium atoms were located at the cerium position or displaced to one of the cube faces. Because the fraction of palladium ions is not large, the direction of Pd^{2+} ions displacement from the cationic position of fluorite is not correlated, which means that the displacement of a particular

palladium ion in any of six possible directions of the (100) family exerts no effect on the displacement direction of the other palladium ions. Thus, when constructing the atomic

model of family 2, the displacement direction for each palladium ion was selected randomly from six possible directions of the (100) family.

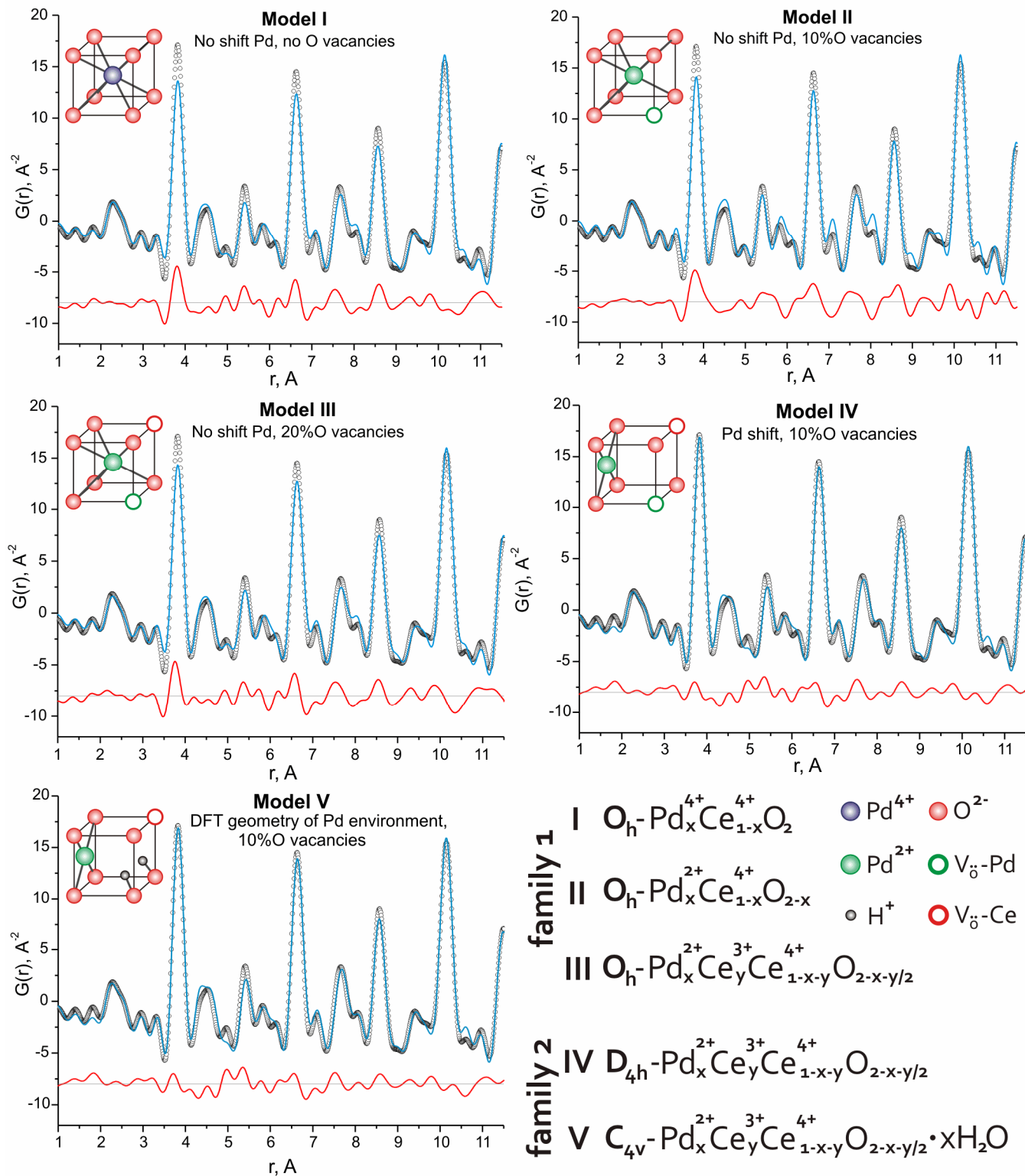


Fig. 9. Experimental PDF curve (circles) for CP-450 sample in the range of scattering vectors $1 < r < 12 \text{ \AA}$, and calculated PDF curves (blue) with the difference curves (red) for all models of the local structure of Pd_xCe_{1-x}O_{2.5} solid solution considered in the study. Schematic representation of the structure of the local environment of the palladium ion within the considered structural models of the Pd_xCe_{1-x}O_{2.5} solid solution and the corresponding gross formulae.

The solid solution cells under consideration are displayed in the Supplementary section (Fig. S5).

The theoretical calculations for these five models, which considered the instrumental resolution and the maximum possible experimental value of Q_{\max} , demonstrated that under the given conditions of the experiment, it is impossible to allocate weak additional peaks that appear due to the displacement of palladium from the fluorite position. However, essential differences in the relative intensity of the peaks attributed to the cationic sublattice can be analyzed. The theoretical PDF curves are presented in the Supplementary section (Fig. S6).

Table 4. Refinement of models I-V for X-ray PDFs of CP-450 sample in the range of interatomic distances $1 < r < 15 \text{ \AA}$.

Model	Pd shift	V_{O} part	R_{wp}	$U(\text{Ce}), \text{ \AA}^{-2}$	$U(\text{Pd}), \text{ \AA}^{-2}$	$U(\text{O}), \text{ \AA}^{-2}$
I	false	0	0.195	0.009	0.008	0.034
II	false	0.1	0.203	0.006	0.034	0.021
III	false	0.2	0.199	0.009	0.011	0.024
IV	true	0.1	0.140	0.009	0.049	0.049
V*	true	0.1	0.141	0.009	0.033	0.037

* This model is based on a geometry of the local environment of the palladium ion, which was obtained by quantum-chemical calculations

The refinement of the structural models with respect to the experimental PDF curve for CP-450 sample is shown in Table 4 and Fig. 9. The smallest R factor was obtained for the family 2 models with the displacement of palladium cations. A distinctive feature of these models is their ability to most correctly describe the intensities of the maxima corresponding to the cation-cation distances. Note that the available instrumental resolution is insufficient for differences in the description of the experiment between models IV and V. Nevertheless, the general formula of the solid solution should be $\text{Pd}_x\text{Ce}_{1-x}\text{O}_{2-x-\delta}$ reflecting the fact that palladium is in ceria lattice in square-planar environment with 2+ oxidation state. Thus the charge compensating oxygen vacancies with mole fraction x are in the bulk of solid solution. Therefore, we will keep the $\text{Pd}_x\text{Ce}_{1-x}\text{O}_{2-x-\delta}$ designation for brevity, where δ – oxygen non-stoichiometry due to the presence of Ce^{3+} ions. It is noteworthy, that the charge compensating vacancies with the mole fraction x can completely or partially be filled with water molecules, in agreement with DFT calculations.

Model V was then taken as the main model for the refinement of the experimental PDF curves for a wide range of interatomic distances. The refinement of the solid solution model with the displacement of palladium cations from the fluorite cell in the range of distances 1-40 \AA is illustrated in Fig. 10.a. The good agreement between the calculated and experimental results and the low R factor (0.157) indicate that the model can adequately describe not only the local but also the average structure. The refined diameter of the solid solution nanoparticles was found to be 6.2 nm. This result agrees well with the CSD size obtained by modeling of the XRD profile (see Table 1).

To relate the proposed model of the solid solution to the data of the standard diffraction experiment, full-profile refinement was

performed using the Model V supercell (Fig. 10.b). At the final step of the refinement, the R factor value was 4.5%. The good agreement between the model and the calculated diffraction patterns indicates that the model of the local structure does not contradict the experimental data for the retained average fluorite structure of the sample. When this diffraction pattern was modeled with the standard CeO_2 structure, at the final step of refinement, we obtained an R factor equal to 4.0% and almost the identical structural parameters. This result demonstrates that for the standard diffraction experiment and refinement of the structure using the Rietveld method, microdistortions occur at the local level upon intercalation of palladium cations into the lattice.

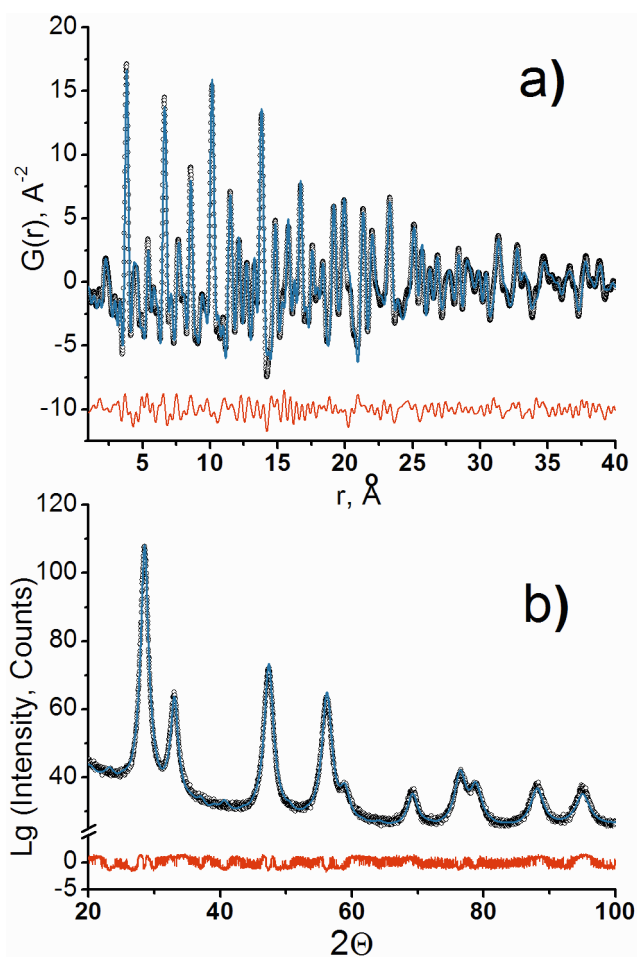


Fig. 10. a) Refinement of the solid solution structure within model V for a wide range of interatomic distances (1-40 \AA) with respect to the X-ray PDF for CP-450 sample. The diameter of the nanoparticles is 6.2 nm. $R_{\text{wp}} = 0.157$. b) Description of the diffraction profile of the CP-450 sample using model V of the solid solution and a $3 \times 3 \times 3$ supercell built from the fluorite unit cells. $R_{\text{wp}} = 0.045$. Designations: (+) – experimental curve, solid red line – calculated curve, solid blue line at the bottom – difference curve.

3.2 Interrelation of the lattice parameter with the size and defects of CeO_2 particles

First, attention should be paid to the increase in the lattice parameter of the fluorite phase that occurs in CP samples upon palladium introduction into the bulk CeO_2 phase. Such data are

regularly reported in the literature by various research teams⁴³⁻⁴⁵. However, according to refs.^{82,83}, a decrease in the particle size of pure CeO₂ below 20 or 12 nm also increases the lattice parameter of these nanoparticles. We have systematized the literature data on the lattice parameter of pure ceria and Pd_xCe_{1-x}O_{2-xδ} solid solutions depending on the particle size and supplemented the experimental data acquired in the present work. As observed in Fig. 11, the lattice parameter increases upon decreasing the crystallite sizes of both the pure ceria and the Pd_xCe_{1-x}O_{2-xδ} solid solutions. The data obtained in the present work show good agreement with the literature which suggests that the formation of the Pd_xCe_{1-x}O_{2-xδ} solid solution cannot be concluded solely from the increased lattice parameter of the fluorite phase. A similar conclusion was made by the authors of⁴⁵.

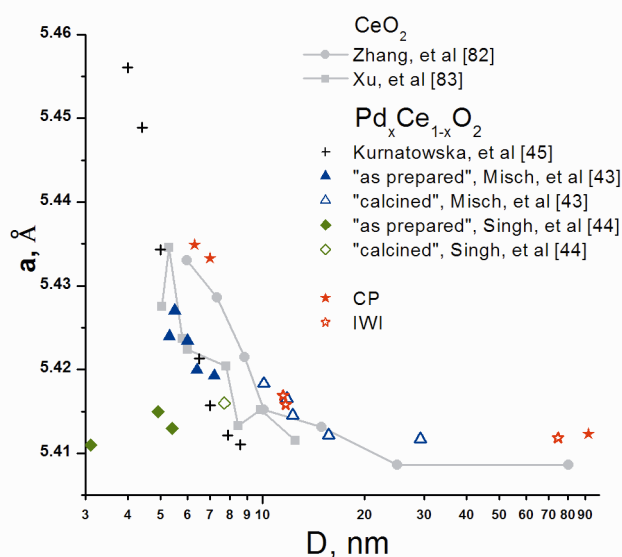


Fig. 11. The lattice parameter of the fluorite phase versus particle size calculated from XRD. The literature data are compared with the data for the samples of CP and IWI series examined in this work.

Quantum-chemical calculations of the solid solution cell demonstrated that the introduction of palladium and a water molecule into the ceria structure would not increase the lattice parameter. The pressure tensor value of -4.18 kbar obtained for the PdO·(CeO₂)₃₁·H₂O solid solution indicates that the CeO₂ lattice parameter should not increase. Thus, the increased value of the lattice parameter of the fluorite phase in the IWI samples can be attributed only to a smaller particle size.

For pure CeO₂, the increase in the lattice parameter is attributed by the authors of⁸³ to an increase in the extent of lattice distortions caused by the growth of the contribution from the surface energy. The XPS data revealed a higher concentration of Ce³⁺ ions and surface carbonate structures for the samples CP-450 and CP-600 compared with the IWI-450 and IWI-600 samples. Such an increased contribution of the Ce³⁺ ions and carbonate/hydroxide species can also be attributed to the smaller particle size of the CP-450 sample compared with IWI-450. We assigned a component with $E_b(O1s) = 531.8$ eV to

the stable surface groups OH⁻ and HCO₃⁻. This assignment does not contradict the data reported in⁸³. An increase in the concentration of surface defects upon decreasing the particle size would increase the concentration of surface groups such as OH⁻ and HCO₃⁻, which are stable in ultrahigh vacuum. Note that an increase in the concentration of surface defects can aid in stabilizing the O₂⁻ radicals at a higher concentration under the action of an oxidizing atmosphere; this effect was observed by ESR in⁸³. Thus, the increase in the lattice parameter of the CP-450 and CP-600 samples with respect to the samples of the IWI series and pure ceria occurs most likely due to a size effect, which can be explained by the great contribution of the surface energy to the total energy of the crystal lattice.

3.3 Coordination of palladium in the CeO₂ structure

Among structural models of such solid solutions discussed in the literature, the best fit to experimental data was demonstrated by the model allowing for the displacement of palladium cations from fluorite positions in the center of an O₈ cube toward one of the faces to provide a transition of palladium from cubic coordination to a near square planar one. Thus, the model predicted in⁴⁸ is supported by our experimental results and calculations. Note that cubic coordination is non-typical of palladium cations and excludes in principle the isomorphic substitution of cerium cations in the fluorite structure. Thus, the square planar coordination of palladium in the solid solution resolves these questions and renders the refined model more acceptable. In addition, because of the absence of correlation effects in the direction of Pd²⁺ ions displacement in the solid solution lattice, the average structure of these solutions is close to the fluorite structure, which explains the absence of additional reflections in the experimental XRD patterns (Fig. 1) obtained for the CP-450 and CP-600 samples. This experimental observation completely agrees with modeling of the XRD pattern for the solid solution cell refined using the XRD-PDF data (Fig. 10 b). It should be emphasized that the absence of additional reflections in the diffraction patterns cannot unambiguously indicate the absence of the dissolution of palladium ions in the structure of ceria or, vice versa, the formation of an isomorphic substitutional solid solution. One can see that non-isomorphic substitution of cerium ions by palladium ions with the formation of a near square planar environment of the latter ones also yields a XRD pattern that is indistinguishable from the corresponding pattern of pure CeO₂. A similar observation were made in⁸⁴ for Ce_{1-x}Sm_xO_{2-δ} nanoparticles, using EXAFS and STEM-EELS the part of Sm atoms was found to be shifted off from the substituted cerium atom position and occupied one neighboring oxygen cube center. Nevertheless, the XRD patterns for Ce_{1-x}Sm_xO_{2-δ} nanoparticles was identical to that one for pure ceria nanoparticles. This feature should be considered when studying such materials using structural methods.

The Raman spectrum for the CP-450 sample reveals an intense and quite narrow band at 187 cm⁻¹ (Fig. 4). As noted above, this band cannot be attributed to CeO₂ or PdO phases. The density of phonon states for palladium oxide, which was

calculated in ⁷⁶, is divided into two separated ranges of 0 – 250 and 450 – 650 cm⁻¹ which correspond to Pd²⁺ and O²⁻ ions due to a pronounced difference in their masses. For this reason, the band at 187 cm⁻¹ is in a frequency range typical for Pd²⁺ ions. However, for pure palladium oxide, the bands at 157 and 168 cm⁻¹ correspond to the IR-allowed modes E_u+A_{2u} for Pd²⁺ ions ⁸⁵, which are Raman-forbidden for palladium ions because Pd²⁺ ions in the P4/2mmc PdO lattice form square-planar [PdO₄] subunits with D_{4h} symmetry. These bands correspond to out-of-plane vibrations of Pd²⁺ ions ⁸⁶. For PdO phase particles the forbidden phonon scattering can be induced by defects or the Fröhlich interactions ⁷⁶, which leads to the appearance of a very weak band at 165 cm⁻¹ for polycrystalline palladium foil compared with Pd(100) single crystal without this band in Raman spectra. Therefore, this mechanism does not explain the high intensity of the band at 187 cm⁻¹ ⁷⁶. However, the 1st coordination sphere of the Pd²⁺ ion in the Pd_xCe_{1-x}O_{2-xδ} solid solution model obtained by DFT calculations is characterized by near square planar geometry with C_{4v} symmetry. The symmetry group C_{4v} is characterized by Raman-allowed vibrations of a central atom with A₁ symmetry. Hence, symmetry lowering of the coordination sphere of the Pd²⁺ ion from D_{4h} to C_{4v} will lead to complete removal of the symmetry restriction and will induce vibrations of the Pd²⁺ ion perpendicular to the 4O²⁻ nearest neighborhoods plane, which will result in the appearance of an intense band in the Raman spectrum. Thus, the band at 187 cm⁻¹ can be assigned to the A₁ vibrations of Pd²⁺ ions in near square planar PdO₄ subunits with the symmetry group C_{4v} in the lattice of the Pd_xCe_{1-x}O_{2-xδ} solid solution. The position of the E_u¹ mode for the PdO phase observed in ⁷⁶ is 165 cm⁻¹, and shown in Fig. 4. One can see that the position of the band A₁ at 187 cm⁻¹ observed for the CP-450 sample differs considerably from the corresponding position for the PdO particles. However, such disagreement can be attributed to a higher value of the force constant. It is known that for covalent bonds, the force constant depends on the bond length as $k(r) \sim r^{-6}$ ⁸⁷. The Pd-O distances obtained by quantum-chemical calculations of the solid solution cell were equal to 1.98 Å, which is less than the Pd-O bond length in pure palladium oxide (2.01 Å). Thus, a decreasing distance between the palladium and oxygen atoms in the solid solution structure would increase the frequency of the appropriate vibrational mode. A rough estimation can be obtained using the formula:

$$\frac{165 [\text{cm}^{-1}]}{(1.98[\text{Å}]/2.01[\text{Å}])^6} = 181 [\text{cm}^{-1}] \quad (5)$$

This estimation yields a theoretical position of this band that is close to the position observed experimentally, thus verifying the quantum-chemical calculations and the assignment of this band precisely to the A₁ vibrational mode of Pd²⁺ ions in the C_{4v} [PdO₄] subunits in the lattice of the Pd_xCe_{1-x}O_{2-xδ} solid solution.

3.4 A comparison with previously developed models

Unfortunately, experimental studies of the local structure of Pd_xCe_{1-x}O_{2-xδ} solutions are quite rare in the literature. Nevertheless, some experimental works elucidating the structure of palladium–ceria solutions were reported in ^{33,37,40}, thus, it is interesting to compare our models with the models proposed in these works. The authors of ³³ performed an EXAFS examination of 1%Pd and 5%Pd/CeO₂ catalysts synthesized by solution combustion and supposed the formation of the Pd_xCe_{1-x}O_{2-xδ} solid solution in which the Pd²⁺ ion substituting for the cerium ion remains in the cerium ion position. Their conclusion appears to be based on some questionable assumptions. In this work ³³, it is proposed that the Pd-O distance in the first coordination sphere of this isomorphous solid solution should be the same as in PdO and equal to 2.02 Å. To obtain this Pd-O distance, the authors assumed that the lattice parameter of the solid solution was 4.67 Å, which is abnormally smaller than the lattice parameter typical of CeO₂, 5.411 Å.

Model I, based on ideal ceria lattice			Model IV, based on ideal ceria lattice			Model V, based on DFT calculated geometry		
Distance	length	c.n.	Distance	length	c.n.	Distance	length	c.n.
Pd-O	2.343	8	Pd-O	1.913	4	Pd-O	1.98	4
Pd-Ce	3.826	12	Pd-O	3.313	8	Pd-H	2.34	2
Pd-O	4.487	24	Pd-Ce	3.025	4	Pd-Ce	3.12	4
			Pd-Ce	4.058	4	Pd-O	3.17	2
			Pd-Ce	4.877	4	Pd-O	3.36	2
			Pd-O	4.278	8	Pd-O	3.41	4
			Pd-O	5.061	8	Pd-O	3.43	2
						Pd-Ce	4.04	4
						Pd-Ce	4.15	1
						Pd-Ce	4.82	1

Fig. 12. The Pd-element bond lengths and respective coordination numbers for an isomorphous substitutional solid solution with the perfect lattice of ceria (model I), a non-isomorphous substitutional solid solution with the perfect lattice of ceria (model IV), and the geometry of the local environment of the palladium ion obtained by quantum-chemical calculations (model V).

For model IV, which is based on the perfect fluorite structure with the displacement of the palladium ion, the 1.913 and 3.313 Å distances appeared naturally (Fig. 12, model IV), without requiring a compression of the lattice from 5.411 to 4.67 Å. The optimized cell geometry, which was obtained by quantum-chemical calculations (Fig. 13, model V), demonstrates that in this case the solid solution structure includes the following distances: the first coordination sphere with coordination number 4 is at a distance of 1.98 Å, and the second coordination sphere includes several close distances: 4 Pd-Ce (3.12 Å), 2 Pd-O (3.17 Å), 2Pd-O (3.36 Å), 2 PdO (3.41 Å) and 2Pd-O (3.43 Å). Thus, our model is in good agreement with the EXAFS data reported in ³³. The authors of ⁴⁰ also examined 2% Pd/CeO₂ samples by EXAFS and observed distances equal to 1.98 Å (coordination number 4.2) and 3.18 Å (coordination number 3.2), which were interpreted within the model of surface Pd-O-Ce superstructures calculated in ³⁷ using the DFT method. The first distance in the model employed by the authors coincides with the Pd-O distances in the first coordination sphere of the solid solution calculated in our work using the DFT method (Fig. 12, model V). One can see that the data reported in ⁴⁰ are described quite accurately by our model V of the bulk solid solution. In contrast to ref. ³⁷, which considers the surface superstructure, we suppose the formation of the bulk disordered solid solution. Nevertheless,

qualitatively our models agree with each other: palladium ions are displaced from the fluorite position with the near square planar environment formation. It cannot be ruled out that superstructures of the type considered in ³⁷ could form on the surface of a bulk Pd_xCe_{1-x}O_{2-x-δ} solid solution.

The proposed solid solution model requires further refinement. First, the positions of the anion sublattice and hydrogen atoms in model V obtained by quantum-chemical calculations should be refined. However, such work and a detailed analysis would require high-resolution neutron scattering experiments and a more comprehensive approach to modeling of the system by, e.g., the inverse Monte Carlo method.

Non-isomorphic substitution of cerium ions by palladium ions naturally produces structural distortions in the parent ceria, which appear as the pronounced microdistortions revealed by the refinement of XRD patterns for CP samples (Table 1). Such distortions may hinder the growth of crystalline domains in the solid solution, which can be considered a main reason for the dispersing effect of palladium on the ceria structure. In addition, this effect of palladium ions on the ceria lattice would increase the lattice oxygen mobility and the OSC value, which is useful for heterogeneous catalysis and can be employed in oxidation reactions.

4 Conclusions

The XRD-PDF method in combination with XPS, HRTEM, Raman spectroscopy, XRD and quantum-chemical calculations was used to investigate a detailed local structure of Pd²⁺ ions in Pd_xCe_{1-x}O_{2-x-δ} solid solutions. The palladium ions were shown to retain the near square planar environment, which is typical of Pd²⁺ ions. The lattice parameter increases due to a decrease in the mean particle size of the Pd_xCe_{1-x}O_{2-x-δ} solid solution rather than due to the substitution of cerium ions by palladium ions. This dispersing effect is provided by distortions of the fluorite structure produced by Pd²⁺ ions. Modeling of the XRD patterns demonstrated that for the non-isomorphic substitution of cerium ions by palladium ions, the average structure of the solution is indistinguishable from the fluorite structure, and no additional reflections are observed in the diffraction patterns. The isolated Pd²⁺ ions, with a near square planar environment in the CeO₂ lattice, can be identified by Raman spectroscopy by the appearance of the band with a Raman shift of 187 cm⁻¹, which corresponds to the A₁ vibrations of palladium ions in C_{4v} [PdO₄] subunits in the ceria lattice. XPS reveals that the state of the Pd²⁺ ion in CeO₂ lattice is characterized by E_b(Pd3d_{5/2}) = 337.9 eV, which exceeds the E_b(Pd3d_{5/2}) value for PdO oxide by 1 eV. The increased value of E_b(Pd3d_{5/2}) for Pd²⁺ in the CeO₂ matrix is related to a decrease in Pd-O distances and the formation of more ionic bonds.

The Pd_xCe_{1-x}O_{2-x-δ} solution is stable and starts to decompose into individual cerium and palladium oxides only upon calcination at 1000°C; this process does not lead to the complete decomposition. The formation of a Pd_xCe_{1-x}O_{2-x-δ} solid solution is a thermodynamically favorable process that occurs even when palladium is deposited on the surface of ceria

by impregnation. The amount of palladium that can dissolve in the ceria lattice during the impregnation is much lower, because an excess of palladium on the surface leads to the formation of small PdO particles with a mean size of approximately 1 nm. For synthesis by coprecipitation, the distribution of palladium is close to equilibrium, and palladium is distributed over the entire volume.

Acknowledgments

Work was supported by RFBR project No 12-03-31613 “My first grant” and Interdisciplinary integration project SB RAS No 124.

Kardash T.Yu. and Stonkus O.A. performed the work in the framework of the joint Research and Educational Center for Energoefficient Catalysis (Novosibirsk State University, Boreskov Institute of Catalysis).

We are grateful to Izaak T.I. for assistance in obtaining Raman spectra

Notes

¹ Boreskov Institute of Catalysis SB RAS, Novosibirsk 630090, Russia

² Novosibirsk State University, Novosibirsk 630090, Russia

* Corresponding author: boronin@catalysis.ru (A.I. Boronin) Boreskov Institute of Catalysis SB RAS, Novosibirsk, Russia. Tel.: +7 3833269631; fax: +7 3833308056

Keywords: palladium, ceria, interaction, solid solution, XRD, pair distribution function, XPS, Raman spectroscopy, DFT.

Electronic Supplementary Information (ESI) available

References

1. A. Trovarelli, *Catalysis Reviews - Science and Engineering*, 1996, **38**, 439-520.
2. E. Schweda and K. Zhenchuan, in *Binary Rare Earth Oxides*, ed. G. Adachi, N. Imanaka and Z. C. Kang, Springer Netherlands, 2005, vol. 1, pp. 57-93.
3. M. Boaro, C. De Leitenburg, G. Dolcetti and A. Trovarelli, *Journal of Catalysis*, 2000, **193**, 338-347.
4. S. Kim, R. Merkle and J. Maier, *Surface Science*, 2004, **549**, 196-202.
5. J. Zhang, H. Kumagai, K. Yamamura, S. Ohara, S. Takami, A. Morikawa, H. Shinjoh, K. Kaneko, T. Adschiri and A. Suda, *Nano Letters*, 2011, **11**, 361-364.
6. D. Terribile, A. Trovarelli, J. Llorca, C. De Leitenburg and G. Dolcetti, *Journal of Catalysis*, 1998, **178**, 299-308.
7. K. Zhou, X. Wang, X. Sun, Q. Peng and Y. Li, *Journal of Catalysis*, 2005, **229**, 206-212.
8. F. Zamar, A. Trovarelli, C. De Leitenburg and G. Dolcetti, *Studies in surface science and catalysis*, 1996, **101 B**, 1283-1292.
9. D. Terribile, A. Trovarelli, J. Llorca, C. De Leitenburg and G. Dolcetti, *Catalysis Today*, 1998, **43**, 79-88.
10. F. Zamar, A. Trovarelli, C. De Leitenburg and G. Dolcetti, *Journal of the Chemical Society, Chemical Communications*, 1995, 965-966.

- 11 H. He, H. X. Dai and C. T. Au, *Catalysis Today*, 2004, **90**, 245-254.
- 12 T. Baidya, G. Dutta, M. S. Hegde and U. V. Waghmare, *Dalton Transactions*, 2009, 455-464.
- 13 A. Gupta, M. S. Hegde, K. R. Priolkar, U. V. Waghmare, P. R. Sarode and S. Emura, *Chemistry of Materials*, 2009, **21**, 5836-5847.
- 14 J.-Y. Luo, M. Meng, X. Li, X.-G. Li, Y.-Q. Zha, T.-D. Hu, Y.-N. Xie and J. Zhang, *Journal of Catalysis*, 2008, **254**, 310-324.
- 15 J.-Y. Luo, M. Meng, J.-S. Yao, X.-G. Li, Y.-Q. Zha, X. Wang and T.-Y. Zhang, *Applied Catalysis B: Environmental*, 2009, **87**, 92-103.
- 16 H. Borchert, Y. Borchert, V. V. Kaichev, I. P. Prosvirin, G. M. Alikina, A. I. Lukashevich, V. I. Zaikovskii, E. M. Moroz, E. A. Paukshtis, V. I. Bukhtiyarov and V. A. Sadykov, *The Journal of Physical Chemistry B*, 2005, **109**, 20077-20086.
- 17 H.-P. Zhou, R. Si, W.-G. Song and C.-H. Yan, *Journal of Solid State Chemistry*, 2009, **182**, 2475-2485.
- 18 B. Yue, R. Zhou, Y. Wang and X. Zheng, *Applied Catalysis A: General*, 2005, **295**, 31-39.
- 19 P. Fornasiero, R. Dimonte, G. R. Rao, J. Kaspar, S. Meriani, A. Trovarelli and M. Graziani, *Journal of Catalysis*, 1995, **151**, 168-177.
- 20 S. Otsuka-Yao-Matsuo, T. Omata, N. Izu and H. Kishimoto, *Journal of Solid State Chemistry*, 1998, **138**, 47-54.
- 21 H. F. Wang, H. Y. Li, X. Q. Gong, Y. L. Guo, G. Z. Lu and P. Hu, *Physical Chemistry Chemical Physics*, 2012, **14**, 16521-16535.
- 22 A. D. Mayernick and M. J. Janik, *J Phys Chem C Nanomater Interfaces*, 2008, **112**, 14955-14964.
- 23 E. Rocchini, M. Vicario, J. Llorca, C. De Leitenburg, G. Dolcetti and A. Trovarelli, *Journal of Catalysis*, 2002, **211**, 407-421.
- 24 A. Gayen, K. R. Priolkar, P. R. Sarode, V. Jayaram, M. S. Hegde, G. N. Subbanna and S. Emura, *Chemistry of Materials*, 2004, **16**, 2317-2328.
- 25 P. Bera, K. C. Patil, V. Jayaram, G. N. Subbanna and M. S. Hegde, *Journal of Catalysis*, 2000, **196**, 293-301.
- 26 Y. Nagai, T. Hirabayashi, K. Dohmae, N. Takagi, T. Minami, H. Shinjoh and S. i. Matsumoto, *Journal of Catalysis*, 2006, **242**, 103-109.
- 27 P. Bera, K. R. Priolkar, A. Gayen, P. R. Sarode, M. S. Hegde, S. Emura, R. Kumashiro, V. Jayaram and G. N. Subbanna, *Chemistry of Materials*, 2003, **15**, 2049-2060.
- 28 A. Bensalem, J.-C. Muller, D. Tessier and F. Bozon-Verduraz, *Journal of the Chemical Society, Faraday Transactions*, 1996, **92**, 3233-3237.
- 29 M. Haneda, T. Mizushima and N. Kakuta, *The Journal of Physical Chemistry B*, 1998, **102**, 6579-6587.
- 30 W.-J. Shen and Y. Matsumura, *Journal of Molecular Catalysis A: Chemical*, 2000, **153**, 165-168.
- 31 R. Craciun, W. Daniell and H. Knözinger, *Applied Catalysis A: General*, 2002, **230**, 153-168.
- 32 S. Golunski, R. Rajaram, N. Hodge, G. J. Hutchings and C. J. Kiely, *Catalysis Today*, 2002, **72**, 107-113.
- 33 K. R. Priolkar, P. Bera, P. R. Sarode, M. S. Hegde, S. Emura, R. Kumashiro and N. P. Lalla, *Chemistry of Materials*, 2002, **14**, 2120-2128.
- 34 A. L. Guimarães, L. C. Dieguez and M. Schmal, *The Journal of Physical Chemistry B*, 2003, **107**, 4311-4319.
- 35 P. O. Thevenin, A. Alcalde, L. J. Pettersson, S. G. Järås and J. L. G. Fierro, *Journal of Catalysis*, 2003, **215**, 78-86.
- 36 G. Glaspell, H. Hassan, A. Elzatahry, V. Abdalsayed and M. El-Shall, *Topics in Catalysis*, 2008, **47**, 22-31.
- 37 S. Colussi, A. Gayen, M. Farnesi Camellone, M. Boaro, J. Llorca, S. Fabris and A. Trovarelli, *Angewandte Chemie International Edition*, 2009, **48**, 8481-8484.
- 38 M. S. Hegde, G. Madras and K. C. Patil, *Accounts of Chemical Research*, 2009, **42**, 704-712.
- 39 M. Cargnello, T. Montini, S. Polizzi, N. L. Wieder, R. J. Gorte, M. Graziani and P. Fornasiero, *Dalton Transactions*, 2010, **39**, 2122-2127.
- 40 S. Hinokuma, H. Fujii, M. Okamoto, K. Ikeue and M. Machida, *Chemistry of Materials*, 2010, **22**, 6183-6190.
- 41 A. Gupta, U. V. Waghmare and M. S. Hegde, *Chemistry of Materials*, 2010, **22**, 5184-5198.
- 42 T. Baidya, K. R. Priolkar, P. R. Sarode, M. S. Hegde, K. Asakura, G. Tateno and Y. Koike, *The Journal of Chemical Physics*, 2008, **128**, 124711-124718.
- 43 L. M. Misch, J. A. Kurzman, A. R. Derk, Y.-I. Kim, R. Seshadri, H. Metiu, E. W. McFarland and G. D. Stucky, *Chemistry of Materials*, 2011, **23**, 5432-5439.
- 44 P. Singh and M. S. Hegde, *Crystal Growth & Design*, 2010, **10**, 2995-3004.
- 45 M. Kurnatowska, L. Kepinski and W. Mista, *Applied Catalysis B: Environmental*, **117-118**, 135-147.
- 46 S. Hosokawa, M. Taniguchi, K. Utani, H. Kanai and S. Imamura, *Applied Catalysis A: General*, 2005, **289**, 115-120.
- 47 Y. Matsumura, W.-J. Shen, Y. Ichihashi and M. Okumura, *Journal of Catalysis*, 2001, **197**, 267-272.
- 48 D. O. Scanlon, B. J. Morgan and G. W. Watson, *Physical Chemistry Chemical Physics*, 2011, **13**, 4279-4284.
- 49 A. B. Kehoe, D. O. Scanlon and G. W. Watson, *Chemistry of Materials*, 2011, **23**, 4464-4468.
- 50 Z. Yang, G. Luo, Z. Lu and K. Hermansson, *The Journal of Chemical Physics*, 2007, **127**, 074704-074705.
- 51 A. D. Mayernick and M. J. Janik, *The Journal of Chemical Physics*, 2009, **131**, 084701-084712.
- 52 M. D. Krcha, A. D. Mayernick and M. J. Janik, *Journal of Catalysis*, 2012, **293**, 103-115.
- 53 M. Nolan, *Journal of Materials Chemistry*, 2011, **21**, 9160-9168.
- 54 T. Egami and S. J. L. Billinge, *Underneath the bragg peaks. Structural analysis of complex materials*, Oxford: Rergamon Press Elsevier, 2003.
- 55 V. I. Korsounski, R. B. Neder, K. Hradil, C. Barglik-Chory, G. Muller and J. Neufelnd, *Journal of Applied Crystallography*, 2003, **36**, 1389-1396.
- 56 H. E. Fischer, A. C. Barnes and P. S. Salmon, *Reports on Progress in Physics*, 2006, **69**, 233.
- 57 S. J. L. Billinge, *Z. Kristallogr*, 2007, **17**.
- 58 E. Mamontov and T. Egami, *Journal of Physics and Chemistry of Solids*, 2000, **61**, 1345-1356.
- 59 M. Coduri, M. Brunelli, M. Scavini, M. Allieta, P. Masala, L. Capogna, H. E. Fischer and C. Ferrero, *Zeitschrift für Kristallographie - Crystalline Materials*, 2012, **227**, 272-279.
- 60 A. I. Boronin, E. M. Slavinskaya, I. G. Danilova, R. V. Gulyaev, Y. I. Amosov, P. A. Kuznetsov, I. A. Polukhina, S. V. Koscheev, V. I. Zaikovskii and A. S. Noskov, *Catalysis Today*, 2009, **144**, 201-211.

- 61 A. S. Ivanova, E. M. Slavinskaya, R. V. Gulyaev, V. I. Zaikovskii, O. A. Stonkus, I. G. Danilova, L. M. Plyasova, I. A. Polukhina and A. I. Boronin, *Applied Catalysis B: Environmental*, 2010, **97**, 57-71.
- 62 E. Slavinskaya, R. Gulyaev, O. Stonkus, A. Zadesenets, P. Plyusnin, Y. Shubin, S. Korenev, A. Ivanova, V. Zaikovskii, I. Danilova and A. Boronin, *Kinetics and Catalysis*, 2011, **52**, 282-295.
- 63 R. V. Gulyaev, A. I. Stadnichenko, E. M. Slavinskaya, A. S. Ivanova, S. V. Koscheev and A. I. Boronin, *Applied Catalysis A: General*, 2012, **439-440**, 41-50.
- 64 A. S. Ivanova, E. M. Slavinskaya, O. A. Stonkus, V. I. Zaikovskii, I. G. Danilova, R. V. Gulyaev, O. A. Bulavchenko, S. V. Tsibulya and A. I. Boronin, *Kinetics and Catalysis*, 2013, **54**, 81-94.
- 65 R. V. Gulyaev, E. M. Slavinskaya, S. A. Novopashin, D. V. Smovzh, A. V. Zaikovskii, D. Y. Osadchii, O. A. Bulavchenko, S. V. Korenev and A. I. Boronin, *Applied Catalysis B: Environmental*, 2014, **147**, 132-143.
- 66 L. S. Kibis, A. I. Titkov, A. I. Stadnichenko, S. V. Koscheev and A. I. Boronin, *Applied Surface Science*, 2009, **255**, 9248-9254.
- 67 T. Skála, F. Šutara, M. Škoda, K. C. Prince and V. Matolín, *Journal of Physics: Condensed Matter*, 2009, **21**, 055005.
- 68 TOPAS 2009 Bruker AXS, 4.2 edn., 1999.
- 69 R. W. Cheary, A. A. Coelho and J. P. Cline, *Journal of Research of the National Institute of Standards and Technology*, 2004, **109**, 1-25.
- 70 X. Qiu, J. W. Thompson and S. J. L. Billinge, *Journal of Applied Crystallography*, 2004, **37**, 678.
- 71 C. L. Farrow, P. Juhas, J. W. Liu, D. Bryndin, E. S. Božin, J. Bloch, T. Proffen and S. J. L. Billinge, *Journal of Physics: Condensed Matter*, 2007, **19**, 335219.
- 72 W. H. Weber, K. C. Hass and J. R. McBride, *Physical Review B*, 1993, **48**, 178-185.
- 73 I. Kosacki, T. Suzuki, H. U. Anderson and P. Colomban, *Solid State Ionics*, 2002, **149**, 99-105.
- 74 Z. Wu, M. Li, J. Howe, H. M. Meyer and S. H. Overbury, *Langmuir*, 2010, **26**, 16595-16606.
- 75 M. Daniel and S. Loidant, *Journal of Raman Spectroscopy*, 2012.
- 76 J. R. McBride, K. C. Hass and W. H. Weber, *Physical Review B*, 1991, **44**, 5016-5028.
- 77 K. Otto, L. P. Haack and J. E. deVries, *Applied Catalysis B: Environmental*, 1992, **1**, 1-12.
- 78 T. Pillo, R. Zimmermann, P. Steiner and S. Hüfner, *Journal of Physics: Condensed Matter*, 1997, **9**, 3987.
- 79 G. B. Hoflund, H. A. E. Hagelin, J. F. Weaver and G. N. Salaita, *Applied Surface Science*, 2003, **205**, 102-112.
- 80 R. J. Farrauto, J. K. Lampert, M. C. Hobson and E. M. Waterman, *Applied Catalysis B: Environmental*, 1995, **6**, 263-270.
- 81 F. Le Normand, J. El Fallah, L. Hilaire, P. Légaré, A. Kotani and J. C. Parlebas, *Solid State Communications*, 1989, **71**, 885-889.
- 82 F. Zhang, S.-W. Chan, J. E. Spanier, E. Apak, Q. Jin, R. D. Robinson and I. P. Herman, *Applied Physics Letters*, 2002, **80**, 127-129.
- 83 J. Xu, J. Harmer, G. Li, T. Chapman, P. Collier, S. Longworth and S. C. Tsang, *Chemical Communications*, 2010, **46**, 1887-1889.
- 84 S.-Y. Chen, R.-J. Chen, W. Lee, C.-L. Dong and A. Gloter, *Physical Chemistry Chemical Physics*, 2014, **16**, 3274-3281.
- 85 G. Kliche, *Infrared Physics*, 1985, **25**, 381-383.
- 86 G. Kliche and Z. V. Popovic, *Physical Review B*, 1990, **42**, 10060-10066.
- 87 W. F. Sherman, *Journal of Physics C: Solid State Physics*, 1982, **15**, 9.